

Scuola di Scienze
Dipartimento di Fisica e Astronomia
Corso di Laurea Magistrale in Fisica

**Characterization of SiPMs
for the Photon Detection system
of the DUNE Far Detector**

Relatore:

Dott. Gabriele Sirri

Presentata da:

Elisabetta Montagna

Correlatori:

Dott. Alessandro Montanari

Dott. Michele Pozzato

*“A billion neutrinos go swimming,
one gets wet.”
Michael Kamakana*

Sommario

Il Deep Underground Neutrino Experiment (DUNE) sarà un esperimento di nuova generazione, con lo scopo di studiare l'oscillazione di neutrini. Esso potrà fornire contributi nel risolvere quesiti ancora aperti come la definizione di una gerarchia di massa e una possibile violazione di CP nel settore leptonic.

L'esperimento prevederà un Near Detector (ND) e un Far Detector (FD), ad una distanza di ~ 1300 km. Il complesso del FD sarà formato da quattro moduli di rivelatore a camere a proiezione temporale riempite di Argon Liquido. Per rivelare la luce di scintillazione emessa in seguito alle interazioni di neutrino all'interno di esse, il Far Detector si avvalerà di un sistema di fotorivelazione composto da collettori di luce accoppiati a fotomoltiplicatori al Silicio (SiPMs).

Questa tesi è incentrata sulle attività di test compiute per verificare la compatibilità dei sensori con le specifiche richieste dall'esperimento necessarie per assicurare l'uniformità di risposta del sistema. In particolare, è presentato uno studio di caratterizzazione completa dei primi campioni di SiPMs, valutando il loro comportamento sia a temperatura ambiente sia in condizioni criogeniche.

Abstract

The Deep Underground Neutrino Experiment (DUNE) is a next generation experiment with the purpose of studying neutrino oscillation. It will contribute in solving some still open questions as a neutrino mass ordering and a possible CP violation in the leptonic sector.

The experiment will be implemented with a Near Detector (ND) and a Far Detector (FD), placed at a distance of ~ 1300 km. The FD complex will be composed of four detectors modules of Liquid Argon Time Projection Chambers. In order to detect the scintillation light emitted by neutrino interactions inside the detector, the FD will make use of a Photon Detection system formed by light collectors coupled to Silicon Photomultipliers (SiPMs).

This thesis is focused on the test activities carried out to verify the compatibility of the photosensors to the experiment requirements necessary to ensure a uniform response of the system. A full characterization of the first SiPM sample is presented, studying their behaviour both at room and in cryogenic environment (77 K).

Contents

Introduction	1
1 Neutrino Physics	3
1.1 Neutrinos in the Standard Model	3
1.2 Massive neutrinos	5
1.3 Neutrino mixing and neutrino oscillation	7
1.3.1 Oscillation in vacuum	7
1.3.2 Oscillation in matter	10
1.4 Neutrino oscillation experiments	11
1.4.1 Solar neutrinos	14
1.4.2 Atmospheric neutrinos	16
1.4.3 Nuclear reactor neutrino	16
1.4.4 Accelerator neutrino	17
1.5 Neutrino mass ordering and CP violation	19
2 The DUNE experiment	21
2.1 The DUNE science program	21
2.2 Long baseline neutrino oscillation physics	22
2.3 Near detector physics	25
2.4 Far detector physics	25
2.4.1 Neutrino interactions	25
2.4.2 Atmospheric neutrinos	26
2.5 Neutrino beam	27
2.6 The Near Detector complex	28
2.7 The Far Detector	30
2.7.1 Single Phase Liquid Argon Time Projection Chamber (SP TPC)	32
2.7.2 Photon detection system	35

CONTENTS

2.7.3	Liquid Argon	38
2.7.4	Dual Phase Time Projection Chamber	39
2.8	DUNE Prototypes	39
3	Silicon Photomultipliers	41
3.1	Silicon photodiodes	41
3.2	Silicon Photomultipliers (SiPMs)	44
3.3	Noise sources in SiPMs	47
3.3.1	Dark current	47
3.3.2	Crosstalk	48
3.3.3	Afterpulsing	49
3.4	SiPMs features at cryogenic temperature	50
4	SiPMs characterization	53
4.1	DUNE requirements	53
4.2	Features of samples tested	55
4.3	Measurements description	56
4.3.1	Setup description	57
4.3.2	Front-end electronics	58
4.3.3	Test equipment	62
4.3.4	Thermal tests	62
4.3.5	I-V curves	65
4.3.6	Dark Count Rate (DCR)	70
4.4	Future objectives	73
	Conclusions	75
	Bibliography	77

Introduction

The *Deep Underground Neutrino Experiment* (DUNE) is an international program which will investigate some open questions in neutrino physics. Despite that neutrino oscillations have been widely studied by several experiments, the neutrino mass ordering and the possible CP violation in leptonic sector are still unresolved.

DUNE will consist of two detectors exposed to an intense neutrino beam. The Near Detector (ND) will be located at Fermilab, Illinois and the Far Detector (FD) at Sanford Lab in South Dakota, at a distance of ~ 1300 km. While the ND will mainly serve as an experiment's control for systematic uncertainties and the beam composition, the FD will consist of four *Time Projection Chambers* (TPC) filled with Liquid Argon (LAr). The design for the first two LArTPC modules will use the Single Phase technology. A prototype detector has been constructed at CERN to test this technology. The topology of a neutrino interaction is reconstructed by looking to the tracks of secondary charged particles which produce scintillation light and free charge carriers by ionization during the propagation in Liquid Argon. The reference time of the event is given by the scintillation light collected by a Photo Detection (PD) system equipped with Silicon PhotoMultipliers (SiPMs) which must work at cryogenic temperature.

In this thesis I was deeply involved in the characterization of the SiPMs and on the verification of the requirements needed by the DUNE Far Detector. A cryogenic test bench has been developed for the measurements at single SiPM level. This is the first step towards a massive test campaign for the mechanical and electrical validation of the full DUNE photosensor sample (~ 300000 devices).

This thesis is organized as follows:

in Chapter 1 a theoretical overview of neutrino oscillation physics is provided along with the main experiments involved in its investigation.

CONTENTS

In Chapter 2 the DUNE experiment is presented. Its scientific program is described along with the physics investigated at the Near and Far Detectors. The Single Phase technology is described in details and the Photon Detection system for the Far Detector is presented with all its components.

In Chapter 3 Silicon Photomultipliers (SiPMs) are described. The working principle and design of this photosensor is reported focusing on the devices features of main importance for DUNE.

In Chapter 4 a description of the SiPMs samples under test and the cryogenic test bench is given. Then, a full characterization of the devices samples is presented, showing the results obtained and how they fulfill the experiment requirements.

Chapter 1

Neutrino Physics

1.1 Neutrinos in the Standard Model

The Standard Model (SM) is a gauge theory based on the symmetry groups $SU(3) \times SU(2) \times U(1)_Y$. In the SM particles are arranged in two main categories: *fermions* (with spin 1/2) and *gauge bosons* (spin 1). Bosons are the mediators of the fundamental interactions: the *photon* for the electromagnetic interaction, W^\pm and Z for the weak and *gluons* for the strong interaction. Fermions are divided into *leptons* and *quarks*, both present into three families. Each charged lepton is coupled to a neutrino of the correspondinty flavour, contributing to create the well-known three families structure of the SM:

$$\begin{pmatrix} e^- \\ \nu_e \end{pmatrix}, \begin{pmatrix} \mu^- \\ \nu_\mu \end{pmatrix}, \begin{pmatrix} \tau^- \\ \nu_\tau \end{pmatrix} \quad (1.1)$$

This structure, of exactly three families, has been confirmed thanks to indirect neutrinos measurements. An extra fermions family of quarks and leptons would also have massless neutrinos which would contribute to the invisible Z decay:

$$Z \rightarrow \bar{\nu}_\alpha \nu_\alpha \quad (1.2)$$

The dependence of the hadronic cross section from the total number of neutrinos' families (N_ν), has been well studied at LEP, obtaining:

$$N_\nu = 2.984 \pm 0.0082 \quad (1.3)$$

The results obtained from the measurements, were in perfect agreement with a three families structure. As shown in Fig.1.1, an additional family would increase the width of the Z resonance and lower the peak, one family less would generate an opposite behavior.

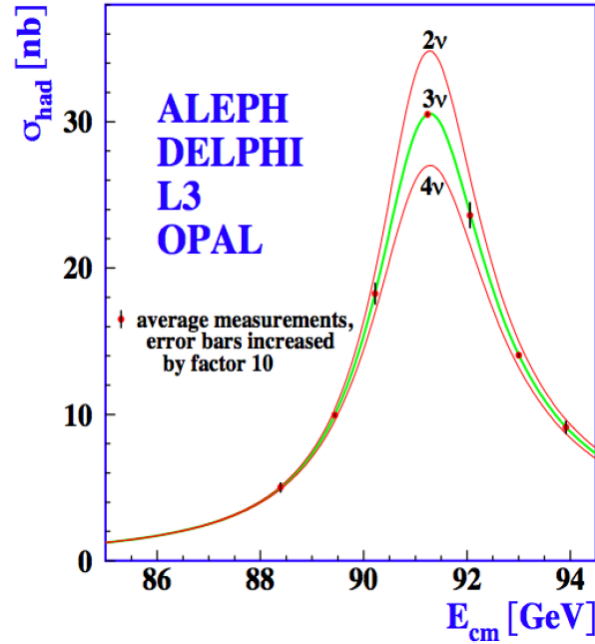


Figure 1.1: Cross section of the hadron production as a function of the center of mass energy, for different N_ν ; the measurements at LEP are compatible with a three families structure of neutrinos.

Neutrinos in the SM are seen as massless and neutral particles, interacting only through the weak interaction. This interaction can be of two type:

- Charged Current (CC), the neutrino is either absorbed or emitted simultaneously with the emission or absorption of the corresponding charged lepton; this kind of interactions happens in the presence of a W^\pm boson;
- Neutral Current (NC), an elastic scattering occurs between the neutrino and another particle, or the creation of a couple neutrino-antineutrino (es. $Z \rightarrow \nu\bar{\nu}$); in this case the interaction is mediated through the neutral boson Z . Unlike the CC interaction, Neutral Current interaction doesn't allow to reconstruct the neutrino's leptonic family of origin.

After different studies of Parity violation in the weak interactions sector and thanks to the Goldhaber experiment about neutrino helicity [2], it appeared clear that only left-handed neutrinos participate in weak interactions. The two component theory of massless neutrino started to form.

It foresees neutrino as a pure left handed helicity state and antineutrino as pure right-handed helicity state. In this way, a right handed term for neutrinos and a left-handed term for antineutrinos are excluded.

Neutrinos in the SM are massless. If this was absolutely true, the Kurie plot of different β decays would be a straight line. However, the presence of a massive neutrino in the decay modifies the end-point of the function (Fig.1.2).

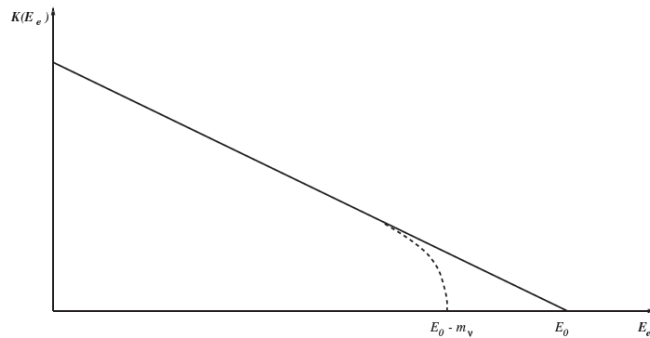


Figure 1.2: Kurie plot: qualitatively different shape of the endpoint of β decay spectrum in presence of non-vanishing neutrino mass.

After studies of the β decay, an upper limit for the neutrino mass has been set. In particular, tritium β decay has been found to be a good process to be observed, in order to set a stringent limit on the neutrino mass. The sensitivity of this kind of measurements will be increased thanks to future experiments as KATRIN [3], which is meant to provide a limit of $m_\nu < 0.2$ eV.

1.2 Massive neutrinos

Particles in the Standard Model gain mass through the Brout-Englert-Higgs (BEH) mechanism. In this process, through Spontaneous Symmetry Breaking, fermions become massive thanks to the interaction between SM bosons and the Higgs boson (and its associated field). However, for what concerns the neutrino scenario, this mechanism keeps neutrinos massless. Evidences of massive neutrinos have been observed from oscillation experiments. Although the nature of this mass is not yet well defined, it has been developed a theory for its construction. Three different scenarios exist for this description.

In the first one neutrino is a Dirac particle. In this approach, the existence of a right-handed neutrino and of a left-handed antineutrino is assumed. The corresponding mass term of the Lagrangian of free fermion, in the case of neutrinos is:

$$\mathcal{L}_m = -m_D(\bar{\nu}_L\nu_R + \bar{\nu}_R\nu_L) \quad (1.4)$$

where, the leptonic number is conserved and neutrino and antineutrino are different particles ($\nu \neq \bar{\nu}$). Following this approach, right-handed neutrinos are called *sterile* neutrinos because they can't interact weakly and left-handed neutrinos are called *active* neutrinos which can be experimentally observed.

In the second scenario neutrino is a Majorana particle. Under this assumption, neutrinos are described using only left-handed components. The mass term of the Lagrangian is:

$$\mathcal{L}_m = -\frac{1}{2}m_M(\bar{\nu}_L^c\nu_L + \bar{\nu}_L\nu_L^c), \quad (1.5)$$

where $\nu^c = C\gamma^0\nu^*$ is the neutrino field term to which has been applied the charge conjugation matrix and $\nu_L^c \equiv (\nu_L)^c = \frac{(1+\gamma_5)}{2}\nu^c$. In this approach, neutrino and antineutrino are the same particle ($\nu = \bar{\nu}$) and the leptonic number is violated.

Another interesting scenario consists in the presence of both the Dirac and Majorana mass term of left chirality, plus a Majorana mass term of right chirality. The Lagrangian for a free neutrino now assumes the form:

$$\mathcal{L} = -\frac{1}{2}(\bar{\nu}_L \quad \bar{\nu}_R^c) \begin{pmatrix} m_L & m_D \\ m_D & m_R \end{pmatrix} \begin{pmatrix} \nu_L \\ \nu_R^c \end{pmatrix} \quad (1.6)$$

where the mass matrix, can be diagonalized through a unitary matrix \mathcal{U} , obtaining on the diagonal the mass terms m_1 and m_2 . The corresponding autovectors are two Majorana mass autostates ν_1 and ν_2 . The mass squared difference can be extracted from the mass matrix:

$$\Delta m^2 = m_2^2 - m_1^2 = (m_L + m_R)\sqrt{(m_L - m_R)^2 + 4m_D^2}. \quad (1.7)$$

This parameter is important in the description of the *mixing* phenomenon.

A particular case of this approach is when $m_L = 0$ e $m_D \ll m_R$. The mass matrix can be diagonalized obtaining:

$$m_1 \simeq \frac{m_D^2}{m_R}, \quad m_2 \simeq m_R \quad (1.8)$$

which is the description of the Type I See-Saw mechanism. Left handed neutrinos masses are zero while right handed neutrinos do not interact through weak interaction. This mechanism creates a heavier neutrino with mass of the order m_R and a lighter one which could represent the experimentally observed one.

1.3 Neutrino mixing and neutrino oscillation

Neutrino masses, whether of Dirac or Majorana type, imply neutrino flavour mixing as happens in the quark sector. For what concerns massive neutrinos, their flavour eigenstates ν_α ($\nu_\alpha = \nu_e, \nu_\mu, \nu_\tau$) do not coincide with the mass eigenstates ν_i ($\nu_i = \nu_1, \nu_2, \nu_3$), but they can be described as a linear combination of them:

$$|\nu_\alpha\rangle = \sum_i U_{\alpha i} |\nu_i\rangle \quad (1.9)$$

where U is the unitary matrix of Pontecorvo-Maki-Nakagawa-Sakata (PMNS). If a mass eigenstate is not degenerate, its phase time evolution will be different from that of the other mass eigenstates. This means that, if at a time t_0 a leptonic state is described by a particular linear combination of mass eigenstates, after a certain time t it will be described by a new linear combination different from that of the leptonic family of origin. This change can produce a periodic variation of the leptonic eigenstates composition, known as the oscillation phenomenon.

1.3.1 Oscillation in vacuum

Considering the oscillation in vacuum, the time evolution of the flavour eigenstates ν_α is:

$$|\nu_\alpha(t)\rangle = \sum_i U_{\alpha i} |\nu_i(t)\rangle \quad (1.10)$$

having assumed the neutrino state as relativistic and as a plane wave:

$$|\nu_i(t)\rangle = e^{-E_i t} |\nu(0)\rangle, \quad (1.11)$$

with energies of the mass eigenstates:

$$E_i = \sqrt{p^2 + m_i^2} \simeq p + \frac{m_i^2}{2p}. \quad (1.12)$$

and same momentum.

The probability that a neutrino of flavour α oscillates into a neutrino of flavour β after a time t is:

$$P(\nu_\alpha \rightarrow \nu_\beta) = |\langle \nu_\alpha | \nu_\beta(t) \rangle|^2 \quad (1.13)$$

which is:

$$= \left| \sum_i U_{\beta i} e^{-E_i t} U_{\alpha i}^* \right|^2 = \sum_i \sum_j U_{\alpha i}^* U_{\beta i} U_{\alpha j} U_{\beta j}^* e^{-(E_i - E_j)t} \quad (1.14)$$

Considering the assumption of relativistic neutrinos, it is assumed $t \simeq L$ and $p \simeq E$. Taking into account the 1.11, the exponent's argument is now:

$$(E_i - E_j)t \simeq \frac{(m_i^2 - m_j^2)}{2p} t \simeq \frac{\Delta m_{ij}^2}{2p} t \simeq \frac{\Delta m_{ij}^2}{2E} L \quad (1.15)$$

where L is the distance travelled by the neutrino, E the neutrino energy and Δm^2 the mass squared difference between two neutrino's mass eigenstates. The oscillation probability can be written as:

$$\begin{aligned} P(\nu_\alpha \rightarrow \nu_\beta) &= \delta_{\alpha\beta} - 4 \sum_{i>j} \text{Re}(U_{\alpha i}^* U_{\beta i} U_{\alpha j} U_{\beta j}^* \sin^2[1.27 \Delta m_{ij}^2 (L/E)]) \\ &\quad + 2 \sum_{i>j} \text{Im}(U_{\alpha i}^* U_{\beta i} U_{\alpha j} U_{\beta j}^* \sin^2[2.54 \Delta m_{ij}^2 (L/E)]). \end{aligned} \quad (1.16)$$

In the simplest case of only two neutrino's families involved in the mixing, the oscillation probability can be simplified as:

$$P(\nu_\alpha \rightarrow \nu_\beta) = \sin^2 2\theta \cdot \sin^2 \left(1.27 \frac{\Delta m^2 [eV^2] L [km]}{E [GeV]} \right). \quad (1.17)$$

It appears clear how the oscillation probability depends on the sinusoidal oscillation $\sin^2 2\theta$ (with θ *mixing* angle) and on the oscillation length L_{osc} which is the distance between two adjacent maximum (or minimum) of the oscillation probability and is defined as:

$$L_{osc} = \frac{4\pi E \frac{\hbar}{c^3}}{\Delta m^2} = 2.48 [km] \frac{E [GeV]}{\Delta m^2 [eV]^2}. \quad (1.18)$$

The probability has a minimum value equal to zero (for $L = 0$ or multiple of L_{osc}) and a maximum value of $\sin^2 2\theta$ (for $L = (n + \frac{1}{2})L_{osc}$) (Fig.1.3). Experiment aimed to study neutrino oscillation have to be realized in order to optimize the ratio L/E with a fixed distance L and energy E ,

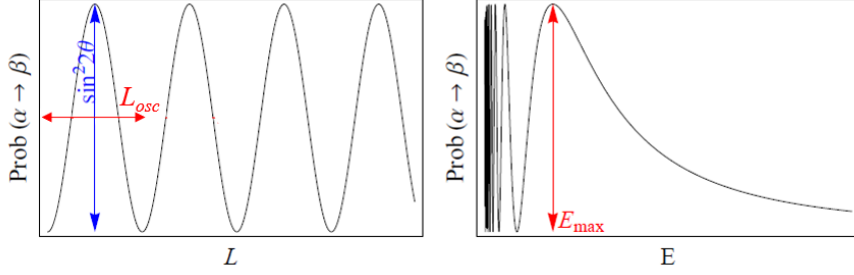


Figure 1.3: Oscillation probability as a function of the baseline L at a fixed neutrino energy in the case of two families (left); same probability as a function of the neutrino energy for a fixed baseline (right).

maximizing the probability to measure a neutrino oscillation; having fixed L and E , the parameter to which a generic experiment is sensitive is the mass squared difference Δm^2 .

A more complete description of the phenomenon extends the case to three neutrinos flavour and can be written with the notation:

$$\begin{pmatrix} \nu_e \\ \nu_\mu \\ \nu_\tau \end{pmatrix} = U_{PMNS} \begin{pmatrix} \nu_1 \\ \nu_2 \\ \nu_3 \end{pmatrix} \quad (1.19)$$

taking use of the Pontecorvo-Maki-Nakagawa-Sakata (PMNS) matrix, of which it is here given a parameterization:

$$\begin{aligned} U_{PMNS} &= \begin{pmatrix} 1 & 0 & 0 \\ 0 & c_{23} & s_{23} \\ 0 & -s_{23} & c_{23} \end{pmatrix} \times \begin{pmatrix} c_{13} & 0 & s_{13}e^{-i\delta} \\ 0 & 1 & 0 \\ -s_{13}e^{i\delta} & 0 & c_{13} \end{pmatrix} \\ &\times \begin{pmatrix} c_{12} & s_{12} & 0 \\ -s_{12} & c_{12} & 0 \\ 0 & 0 & 1 \end{pmatrix} \times \begin{pmatrix} 1 & 0 & 0 \\ 0 & e^{i\alpha_1} & 0 \\ 0 & 0 & e^{i\alpha_2} \end{pmatrix} \end{aligned} \quad (1.20)$$

where c_{ij} and s_{ij} are $\cos \theta_{ij}$ and $\sin \theta_{ij}$ of the mixing angles, δ is a Dirac phase associated with the CP violation in the leptonic sector and α_i ($i = 1, 2$) are the Majorana phases. Studying neutrino oscillation we refer to a specific matrix of the ones reported above basing on the different sector: parameters involved in atmospheric neutrino oscillations are contained in the first matrix, in the case of neutrinos from reactor we refer to the second one, parameters of the third can be investigated in the solar neutrino sector while the last matrix contains the Majorana phases which cannot be studied by neutrino oscillation but with, for example, the neutrinoless double beta decay.

1.3.2 Oscillation in matter

A different description is required for the more general case of neutrino propagation in matter, although the probability of neutrino interaction is very low. The coherent forward neutrino scattering with nucleons and electrons contained in matter can modify the amplitude of the neutrino propagation. This scattering can be induced by both a charged current (CC) and neutral current (NC) interaction, but: while for all kind of neutrino flavours it is possible to have NC interactions with matter, CC interactions are possible only for electron neutrinos ν_e (Fig.1.4), therefore the effect on the propagation depends on the neutrino flavour. This effect, called Mikheyev-Smirnov-Wolfenstein (MSW) effect, can be described by an effective potential that depends on the density of the matter. In the case of ν_e , the effective potential due to CC interactions can be written as:

$$V_{CC} = \pm\sqrt{2}G_F n_e \quad (1.21)$$

where G_F is the Fermi constant and n_e is the electron density of the medium. For the case of ν_μ and ν_τ the potential due to CC interactions is zero since matter does not contain the corresponding charged leptons, so there is only the contribution of NC interactions with neutrons:

$$V_{NC} = \mp\frac{\sqrt{2}}{2}G_F n_n \quad (1.22)$$

where G_F is the Fermi constant and n_n is the neutron density of the neutral medium.

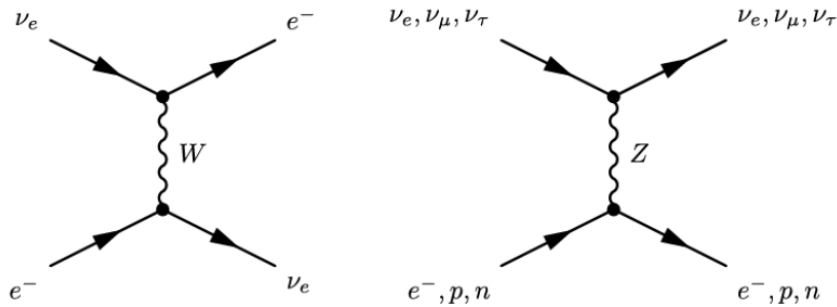


Figure 1.4: Feynman diagram of Charged Current interaction (left) and Neutral Current interaction (right) in matter. CC interactions are possible only for ν_e due to the lack of μ and τ in the medium.

1.4 Neutrino oscillation experiments

In the description of the experimental scenario of neutrino oscillation study, it is useful a first main distinction. There are two kind of experiments: the *appearance* and the *disappearance* ones. In the first case, knowing the initial neutrino flavour observed from a source, the probability of appearance of a different flavour after traveling a certain distance L is searched for. In the second one, a decrease in the flux of a certain neutrino flavour generated at the source is observed and its survival probability is studied.

Neutrino experiment can make use of different neutrino sources which can be divided in the following groups:

- **solar neutrinos:** produced by the fusion reactions that happen in the Sun, they are of electron flavour only. The great majority of the solar neutrinos comes from the pp reaction $p+p \rightarrow {}^2\text{H}+e^++\nu_e$, other reactions produce neutrinos but very fewer (Fig.1.5). The entire pp cycle which happens inside the Sun, can be summarized by the reaction: $4p \rightarrow {}^4\text{He} + 2e^+ + 2\nu_e$. The main energy of solar neutrinos is $\langle E_\nu \rangle \simeq 0.42$ MeV and, basing on the Standard Solar Model (SSM), the expected flux which can reach the Earth is $\Phi_{\nu_e} = 6 \times 10^{10} \text{cm}^{-2}\text{s}^{-1}$ [4];

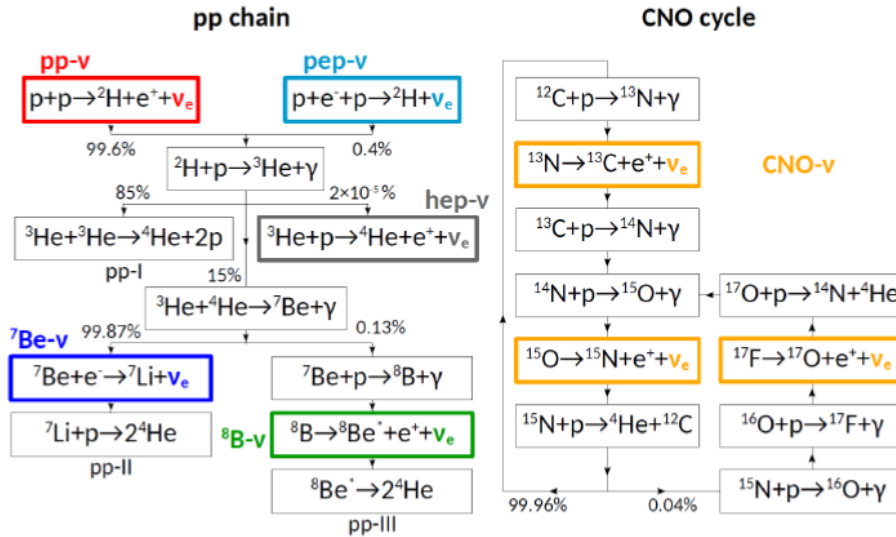


Figure 1.5: Different cycles for solar neutrino production.

- **atmospheric neutrinos:** produced by the interaction of Cosmic Rays (CR) in the upper atmosphere. The resulting adronic shower,

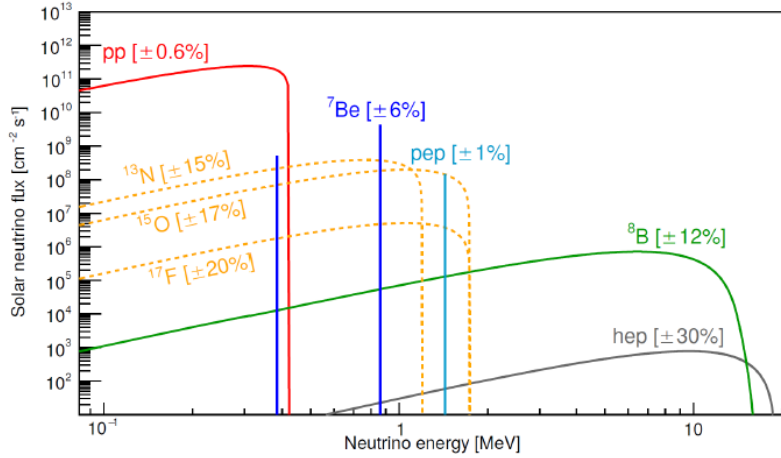


Figure 1.6: The energy spectrum of solar neutrinos arriving on Earth along with standard solar model uncertainties. The abbreviation refer to the reaction shown in Fig.1.5. The dashed lines represent the neutrinos coming from the CNO cycle. The solid line indicate neutrinos coming from the main reactions of the pp cycle. The numbers shown are the theoretical errors of the fluxes.

contains particles (as pions or kaons) which can decay before reaching the Earth surface ($\pi^+ \rightarrow \mu^+ \nu_\mu$, $K^+ \rightarrow \mu^+ \nu_\mu$ and then $\mu^+ \rightarrow e^+ \nu_e \bar{\nu}_\mu$), creating neutrinos and antineutrinos (Fig.1.7). Considering the CRs' composition, atmospheric neutrinos are both electron and muon type. Without oscillation, for energy below the GeV, the ratio between the two flavour has been estimated to be:

$$R_{\mu/e} = \frac{\nu_\mu + \bar{\nu}_\mu}{\nu_e + \bar{\nu}_e} \simeq 2 \quad (1.23)$$

Basing on the arrival direction, atmospheric neutrinos can be divided into: *downgoing*, traveling a distance of 10-20 km in atmosphere above the observation point and *upgoing*, coming from the opposite side of the observer traveling for $L \sim 10^4$ km through the Earth (Fig.1.8). At energy of about GeV the earth absorption is negligible and the neutrino flux, being isotropic and assuming no oscillation, should be the same in the two cases.

- **nuclear reactor neutrinos:** they are electron antineutrinos ($\bar{\nu}_e$) produced by the β^- decay of fission products. The energy E_ν is of the order of few MeV and it is uniformly distributed over the total solid angle. Even in presence of neutrino oscillations, due to the low energy of $\bar{\nu}_e$, it is not possible to observe the appearance of $\bar{\nu}_\mu$ and $\bar{\nu}_\tau$. This is because the energy threshold for the τ^+ and μ^+ production

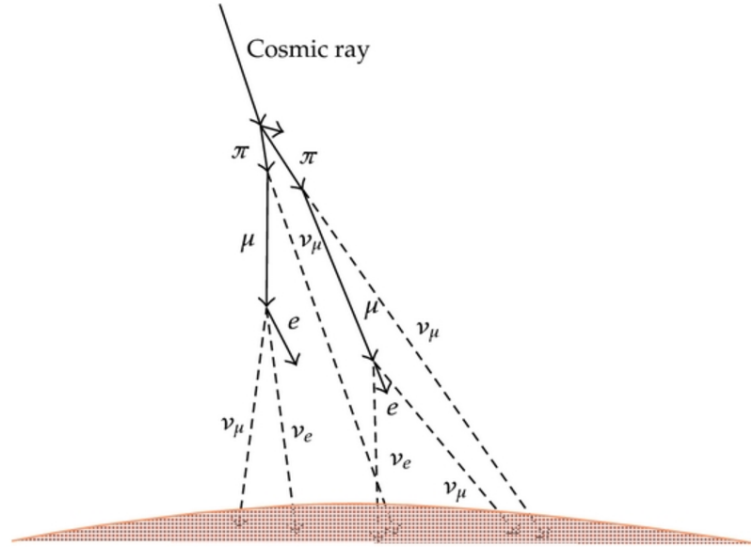


Figure 1.7: Cosmic Rays interaction with the upper atmosphere.

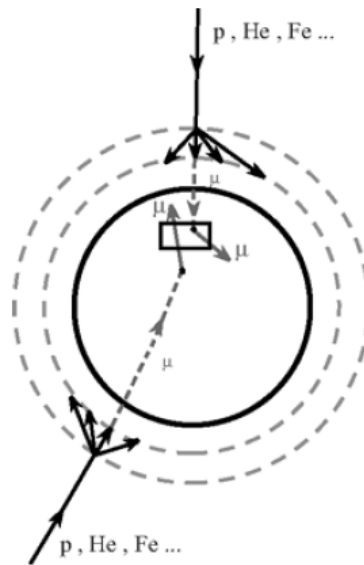


Figure 1.8: Arrival direction for *downgoing* or *upgoing* atmospheric neutrinos produced in the CR interaction with the atmosphere.

is too high for the process. Experiments which use nuclear reactor neutrinos are of the *disappearance* type. Neutrino oscillation study in this kind of experiments is carried out comparing the observed rate of positrons from the inverse β decay and the predicted one (or that measured before the oscillations).

- **neutrinos from accelerator:** accelerated high energy protons onto a nuclear target produce secondary particles, as pions and kaons, which can decay into final states containing ν_μ or $\bar{\nu}_\mu$ ($\pi^+, K^+ \rightarrow \mu^+ \nu_\mu$ and $\pi^-, K^- \rightarrow \mu^- \bar{\nu}_\mu$). It is possible to create muonic beams with energy of few GeV, the purity of which is limited by neutrinos and antineutrinos coming from the muon decay ($\mu^+ \rightarrow e^+ \bar{\nu}_\mu \nu_e$ and $\mu^- \rightarrow e^- \nu_\mu \bar{\nu}_e$). Experiments which make use of this kind of source are called *long baseline* or *short baseline* depending on the flight length.

1.4.1 Solar neutrinos

Many experiments have been studied solar neutrinos for decades. Along with reactor neutrinos experiments, they are sensitive to Δm_{21}^2 and $\sin^2 2\theta_{21}$. The pioneering one was designed by the astrophysicist R. Davis in Homestake, South Dakota. Its purpose was the measurements of the flux of solar neutrinos coming from the fusion reactions in the Sun and compare it to the theoretical one. To achieve this, a deep underground target containing ^{37}Cl was used exploiting the absorption of ν_e through the CC reaction:



the ^{37}Ar nuclei produced are radioactive and after a certain exposure time they were chemically extracted to be introduced in a proportional counter used to detect their decay. In this way, the number of solar neutrino captured was reconstructed. The resulting measured neutrinos flux was one third of the predicted one giving start to the "solar neutrino problem".

Other two important experiments were GALLEX/GNO (at Gran Sasso, Italy) and SAGE (at Baksan, Russia). Both of them were radiochemical experiments exploiting the reaction:



the ^{71}Ge atoms decay through electron capture. These two experiments too measured a reduction in the solar neutrinos flux.

All of the experiments described above proved the evidence of a "lack" of solar neutrinos respect to the theoretical models, but no one of them

could prove that this deficit was the result of the neutrino oscillation phenomenon. The decisive contribution came from the SNO (Sudbury Neutrino Observatory) experiment, in Canada. In fact, it was not only able to measure the ν_e flux, but also to reconstruct the contribution of the oscillated ν_μ and ν_τ from solar neutrinos. SNO was a spherical detector filled up with one kilo tone of heavy water to detect the Cherenkov light emitted from charged particles going through; it was also shielded by 1.5 kilo tones of normal water. There were three possible reaction to study:

- **Electron Scattering:**

$$\nu_x + e^- \rightarrow \nu_x + e^-; \quad (1.26)$$

this channel is sensible to all kind of neutrino flavours but is mostly dominated by ν_e interactions due to the reduced cross section of the others neutrinos.

- **Charged Current** (inverse β decay):

$$\nu_e + p \rightarrow e^- + n; \quad (1.27)$$

possible only for ν_e through W^\pm which allows to measure the flux $\Phi_{\nu_e} = \Phi_{CC}$.

- **Neutral Current** (possible for all neutrino flavours):

$$\nu_x + d \rightarrow \nu_x + p + n; \quad (1.28)$$

in which an atom of Deuterium is dissociated through the exchange of a Z^0 ; the neutron produced by this dissociation could be captured emitting a photon which was being observed. This allowed to measure the total flux $\Phi_{\nu_e+\nu_\mu+\nu_\tau} = \Phi_{NC}$, of particular importance to prove that, while a determine flavour undergoes an oscillation, the total expected flux is still preserved .

Thanks to this particular configuration of the experiment, it was possible to measure the ratio Φ_{CC}/Φ_{NC} of $\sim 1/3$ giving a proof for solar neutrino oscillation.

Another important experiment to mention is Borexino. Located at the LNGS, it has been specifically desinged to observed low energy neutrinos. Among its results there are: the first direct spectroscopy of solar neutrinos from the pp interaction, the interaction rate for solar neutrinos from ${}^7\text{Be}$, the first direct measure of solar neutrinos flux from pep and the measure of the interaction rate for solar neutrinos from ${}^8\text{Be}$ with low energy threshold.

1.4.2 Atmospheric neutrinos

Experiment which study this kind of source, as well as accelerator neutrinos ones, are sensitive to $\Delta m_{31(32)}^2$ and $\sin^2 2\theta_{31(32)}$.

Atmospheric neutrino oscillation could manifest as a discrepancy between the expected and the measured value of the ratio R described by (Eq.1.23). Different experiments have been designed for the study of the atmospheric neutrino sector, among them: Super-K (SK), MACRO and Soudan-2.

Super-K, at a depth of 1000 meters in the Kamioka mine in Japan, consists in a large water Cherenkov detector [5]. It has been able to measure neutrino fluxes as functions of the zenith angle (θ), showing a decrease for the *upgoing* ν_μ flux ($\cos\theta < 0$) respect to the predicted one with no oscillation.

MACRO was a large underground apparatus at the LNGS in Italy [4]. The detector had a modular structure of three sub-detectors: liquid scintillators counters, layers of limited streamer tubes interleaved with passive material and nuclear track detectors. The tracking was performed using the hits in the streamer tubes. The time information, provided by scintillation counters, allowed the determination of the direction by the time-of-flight measurements. This made the detector able to measure different class of atmospheric neutrino interactions. In searching for evidences for neutrino oscillation, considering the best-fit parameters $\sin^2 2\theta = 1$ and $\Delta m^2 = 2.5 \times 10^{-3} eV^2$, the measured deficits for *upgoing* neutrinos were consistent with the hypothesis of $\nu_\mu \rightarrow \nu_\tau$.

Soudan-2, at the Soudan mine in the United States, also observed the atmospheric neutrino oscillation effects. It was originally designed to observe proton decay with atmospheric neutrinos only being part of the background signal, as other experiments of this kind. It is an iron tracking calorimeter with a particular honeycomb geometry which operates as a time projection chamber. Soudan-2 has been able to measure the flux ratio $\nu_\mu/\nu_e = \Phi(\nu_\mu + \bar{\nu}_\mu)/\Phi(\nu + \bar{\nu}_e)$ and compare it with the one predicted from Monte Carlo simulations, resulting in a good agreement with the hypothesis of $\nu_\mu \rightarrow \nu_\tau$ oscillation [6].

1.4.3 Nuclear reactor neutrino

Nuclear reactors produce $\bar{\nu}_e$ flux with energy < 10 MeV making their disappearance the only channel accessible with these sources. Goal of these kind of experiment is to compare the observed rate of positrons from the inverse β -decay to the predicted one. The signature is the coincidence of a

prompt positron and a delayed neutron; by searching for it, it is important to have also a good background signal rejection.

Two experiments which made use of nuclear reactor neutrino were Chooz and Palo Verde. They were short baseline experiments with a baseline distance of $L \sim 1$ km, which makes the $\bar{\nu}_e$ oscillation driven by Δm_{12}^2 negligible, while allows direct measurement of $\sin^2\theta_{13}$. Both of them found no evidence for $\bar{\nu}_e$ disappearance obtaining a limit of $\sin^2 2\theta_{13} < 0.1$ at 90 %CL.

After these initials contribution, other three new nuclear reactor similar experiments have been realized: Double Chooz (France), RENO (Korea) and Daya Bay (China) [8]. Among them, a significant contribution in determining $\sin\theta_{13}$ has come from Daya Bay. The experiment has accumulated the largest reactor antineutrino sample in the world and has obtained the measure $\sin^2 2\theta_{13} = 0.084 \pm 0.005$ with a data acquisition of 621 days in 2015[9].

An important contribution to mention comes from the KamLAND experiment. Being a long-baseline reactor experiment with $L \sim$ few hundreds of km, it is sensible to Δm^2 down to 10^{-5} eV². KamLAND is located underground in the old Kamiokande's site in Japan surrounded by different nuclear reactors which produce the $\bar{\nu}_e$ flux to be observed. The analysis obtained combining Kamland measurements with those of solar neutrino experiments, gives as results for the oscillation parameters $\Delta m_{21} = 7.59_{-0.21}^{+0.21} \times 10^{-5}$ eV² and $\tan^2\theta_{12} = 0.47_{-0.05}^{+0.06}$ [11].

1.4.4 Accelerator neutrino

An intense protons beam colliding onto a nuclear target can be used to produce neutrino beams. Mesons (in particular pions), are created from the proton collision. Secondary pions are focused towards a "decay tunnel" using magnetic horns making also possible a sign selection of them. They decay then in a decay pipe or tunnel producing muon neutrinos or antineutrinos. A muon absorber is placed at the end of the tunnel to stop the muon component of the decay. It is possible to control important features of the neutrino beam by choosing the energy and intensity of the primary proton beam and other settings of the beam facility. In addition, the arbitrarily distance between source and detector, makes these kind of experiments very effective in studying desired oscillation parameters.

Many of the modern long baseline neutrino experiments are composed by a "near" and a "far" detector. The near detector allows to measure the unoscillated neutrino flux immediately after the production. The far detector analyzes the flux after a possible flavour oscillation.

Long baseline accelerator experiments, with typically $E \sim 1$ GeV and $L \sim 10^3$ km, can explore region of $\Delta m^2 \geq 2 \times 10^{-3} eV^2$.

The KEK-to-Kamioka (KEK) long baseline neutrino oscillation experiment was the first one. A muon neutrino beam with $\langle E_\nu \rangle \sim 1.3$ GeV was produced by the KEK-Proton Synchrotron towards the Super-Kamiokande detector at a distance $L=250$ km. A near detector located 300 m far from the production target was also used. The analysis performed combining measurements from the far and the near detector confirmed the atmospheric neutrino oscillation.

The second long baseline neutrino experiment with a two detector designed was MINOS. A beam of neutrinos produced by the NuMI (Neutrinos at the Main Injector) facility was sent from the FNAL (Fermi National Accelerator Laboratory) towards a detector located in the Soudan Mine at a distance of 735 km. The far detector, located underground, was a iron-scintillator tracking calorimeter with a total mass of 5.4 kton. The near detector was also an iron-scintillator calorimeter but with a total mass of 0.98 kton. Both of them presented a toroidal magnetic field. MINOS confirmed the muon neutrino disappearance in this case also obtaining $\Delta m^2 = (2.43 \pm 0.13) \times 10^{-3} eV^2$ (68% CL) and $\sin^2(2\theta) > 0.90$ (90% CL) [10].

A narrow ν_μ spectrum can be produced by directing the beam off-axis with a defined angle. The T2K (Tokai to Kamioka) long baseline experiment is the first one designed using an off-axis beam. T2K makes use of neutrino beam with a peak energy of 0.6 GeV and directs it to the SK detector with a 2.5° off-axis angle, over a distance of 295 km. It started taking data since 2010 and has been the first experiment to provide an observation of $\nu_\mu \rightarrow \nu_e$ oscillations.

NO ν A is an off-axis neutrino experiment and represents the MINOS successor. Its detectors are placed 14.6 mrad off-axis. Both the near and the far detectors are fine grained tracking calorimeters composed by arrays of PVC cells filled with liquid scintillator. The baseline distance is of 810 km. NO ν A is dedicated to precision measurements of ν_μ ($\bar{\nu}_\mu$) disappearance probability and ν_e ($\bar{\nu}_e$) appearance probability[7].

The OPERA experiment was designed to demonstrate the ν_τ appearance in a muon neutrino beam. To reach the τ production threshold of $\langle E_\nu \rangle \sim 3.5$ GeV, a high-energy neutrino beam was requested. The muon neutrino source was located at CERN while the detector was underground at the LNGS, over a distance of 730 km. The CNGS (CERN to Gran Sasso) neutrino beam was produced by the CERN SPS with a $\langle E_\nu \rangle = 17$ GeV. The detector was a hybrid of Emulsion Cloud Chambers (ECC) and a magnetized spectrometer. The OPERA collaboration observed a total

of 10 events of ν_τ appearance concluding its discovery with a significance larger than 5σ [8].

Table 1.1: Summary of different neutrino oscillation experiments along with some of their main features.

Source	Experiment	ν Flavour	\bar{E} (GeV)	L (km)	$\Delta m_{min}^2 (eV^2)$
Reactor	Chooz	$\bar{\nu}_e$	10^{-3}	1	10^{-3}
Reactors	KamLand	$\bar{\nu}_e$	10^{-3}	100	10^{-5}
Accelerator	Chorus,Nomad	$\nu_\mu, \bar{\nu}_\mu$	1	1	~ 1
Accelerator	K2K,MINOS,Opera	$\nu_\mu, \bar{\nu}_\mu$	1	300-700	10^{-3}
Atmospheric	SK,Soudan	$\nu_{\mu,e}, \bar{\nu}_{\mu,e}$	1	$10 - 10^4$	$10^{-1} - 10^{-3}$
Atmospheric	SK,MACRO	$\nu_\mu, \bar{\nu}_\mu$	10	$10^2 - 10^4$	$10^{-1} - 10^{-3}$
Solar	SK,SNO,Gallex	ν_e	10^{-3}	10^8	10^{-11}

1.5 Neutrino mass ordering and CP violation

The existence of massive neutrinos implies a change in the Standard Model. Oscillation experiments allow to measure the mass squared difference but not their individual masses. From the existing data, it is now known the value of Δm_{21}^2 and $|\Delta m_{31}^2|$. The sign of $|\Delta m_{31}^2|$ is still unknown. This generates a problem in determining the neutrino mass ordering. In the case of a three neutrino mixing, the two possible sign of $|\Delta m_{31}^2|$ correspond to two different mass ordering. Assuming m_1 as the mass eigenstates with the largest mixing with the electron neutrino flavour (Fig.1.9):

- **Normal Ordering (NO):**

$$m_1 < m_2 < m_3, \quad \Delta m_{31}^2 = \Delta m_{atm}^2 > 0, \quad \Delta m_{21}^2 = \Delta m_{\odot}^2 > 0; \quad (1.29)$$

- **Inverted Ordering (IO):**

$$m_3 < m_1 < m_2, \quad \Delta m_{32}^2 = \Delta m_{atm}^2 < 0, \quad \Delta m_{21}^2 = \Delta m_{\odot}^2 > 0. \quad (1.30)$$

One of the main goals of future research program is to unveil the correct ordering.

An upper limit on the sum of neutrinos masses is obtained from cosmological studies. The actual limit combining different measurements and models is:

$$\sum_j m_j < 0.170 \text{ eV}, \quad 95\% \text{ CL}. \quad (1.31)$$

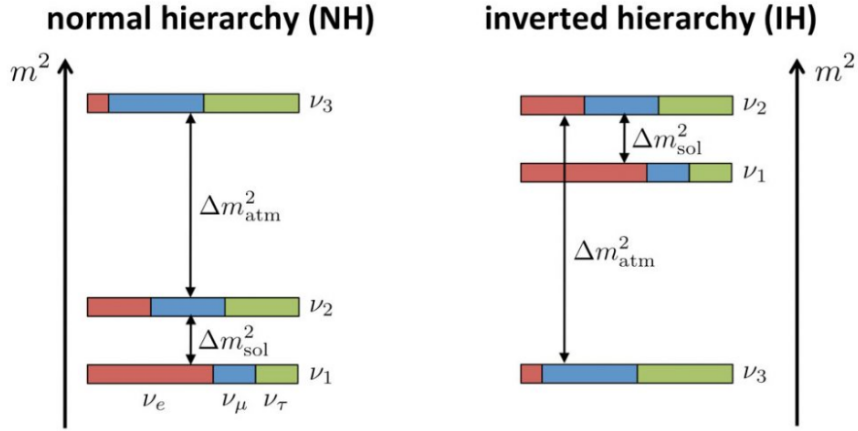


Figure 1.9: The two possible mass ordering in the case of three active neutrinos.

The CP violation in the lepton sector is still another important sector to be studied. In the neutrino oscillation study the CPV phases present in the mixing matrix U_{PMNS} are of particular interest.

A measurement of the value of $\delta_{CP} \neq 0$ or π , assuming that neutrino mixing follows the three-flavor model, would imply CP violation. The non zero δ_{CP} term can manifest itself as a difference in the oscillation probability between neutrinos and antineutrinos. In appearance experiment, in the case of a two flavour mixing, the CP asymmetry is [12]:

$$\mathcal{A}_{CP} = \frac{P(\nu_\alpha \rightarrow \nu_\beta) - P(\bar{\nu}_\alpha \rightarrow \bar{\nu}_\beta)}{P(\nu_\alpha \rightarrow \nu_\beta) + P(\bar{\nu}_\alpha \rightarrow \bar{\nu}_\beta)} \quad (1.32)$$

A non zero value of these term could provide the CP violation necessary in the leptogenesis for the generation of the observed baryon asymmetry of the Universe.

A similar effect occurs because of the matter effect. Its origin is simply in the presence of only electrons and absence of positrons in the Earth. For energies in the GeV range, the asymmetry from the matter effect increases with baseline as the neutrinos pass through more matter. Some experiments can exploit this feature, by choosing a longer baseline which makes them more sensitive to the neutrino mass ordering.

Chapter 2

The DUNE experiment

2.1 The DUNE science program

The Deep Underground Neutrino Experiment (DUNE) is an international future project focused on studying neutrino physics, located in the U.S. . It will be designed as a long baseline experiment consisting of a Far Detector (FD) and a Near Detector (ND). While the ND will be housed at FermiLab, the FD will be located underground at the Sanford Lab in South Dakota, at a distance of ~ 1300 km (Fig.2.1).

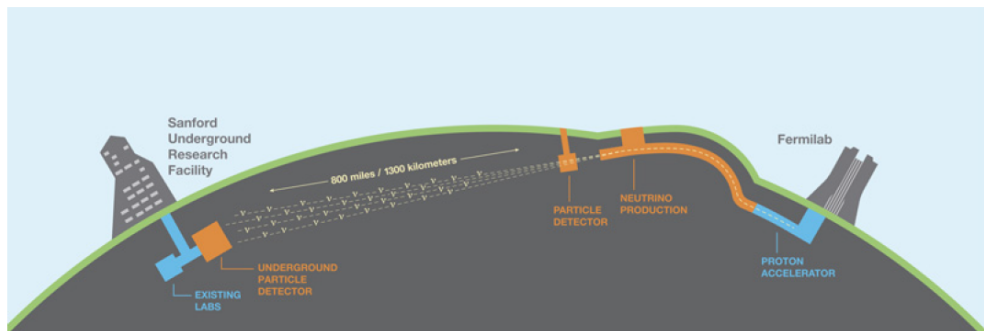


Figure 2.1: Scheme of the DUNE long-baseline design.

Purpose of the experiment will be to study the still open questions of neutrino physics, as [19]:

- matter-antimatter asymmetry in the early Universe. The dominant role of matter in today's Universe is clear but the mechanism which creates this asymmetry at the beginning is still unknown. With its high sensitivity, DUNE could contribute in solving this mystery

through the studying of charge-parity symmetry violation (CPV) in neutrino flavour mixing.

- the dynamics of the supernova neutrino bursts (SNBs). DUNE is capable of collecting and analyzing neutrinos coming from the core-collapse of a Supernova within the Milky Way. This could provide an opportunity in studying the evolution of the Universe as well as neutron stars or black holes formation.
- protons decay and the existence of a Grand Unified Theory (GUT). The theory which describes the unification of the known forces predicts also the rates for the proton decay. The DUNE experiment will search for this type of decay during its activity program.

Primary objectives of the experiment will be to study some of the main features of neutrino oscillation. By analyzing the parameters involved in the $\nu_\mu \rightarrow \nu_e$ oscillations, it will be possible to obtain: precision measurements of the third mixing angle θ_{13} , measurements of the CP violating phase δ_{CP} and the determination of the neutrino mass ordering. It will be possible to have precision measurement of the third mixing angle θ_{23} as well as determine the value of the mass squared difference $|\Delta m_{23}^2|$. Search for proton decay will also be carried out by analyzing different candidate decay modes, as for example: $p \rightarrow K^+\bar{\nu}$. Finally, if a core-collapse supernova should occur during the life time of the experiment, it will be possible to detect the neutrino flux coming from it. This could represent an important contribution in the study of stellar evolution in our Galaxy.

DUNE's science program will also include some ancillary research items. Thanks to the experiment's sensitivity, it will be possible to search for Beyond the Standard Model phenomena. Some fields of this BSM physics investigated will be: active-sterile neutrino mixing, non-standard interactions, light-mass dark matter etc. Oscillation from atmospheric neutrinos will be also under study along with some other measurements of astrophysical phenomena.

2.2 Long baseline neutrino oscillation physics

The DUNE experiment will be design with a baseline of 1300 km between its two detector sites. This peculiarity is of great importance for the accomplishment of some of the expected objectives. One of them is the study of the matter-antimatter asymmetry. As described in section

1.5, studying neutrino oscillation, there are two main contributions for this asymmetry coming from the CP violation and the matter effect.

For the CPV contribution, if $\delta_{CP} = 0$ or π , the transition probability for oscillation in vacuum is the same for neutrinos and antineutrinos. Otherwise, for value of $\delta_{CP} \neq 0, \pi$, the term would cause a difference in the probabilities for $\nu_\mu \rightarrow \nu_e$ and $\bar{\nu}_\mu \rightarrow \bar{\nu}_e$ transitions. This asymmetry is described by the Eq. 1.32.

In the case of oscillations in matter, the MSW effect creates a difference between the neutrino and antineutrino probabilities, even for $\delta_{CP} = 0$ or π . The matter effect can be exploited to study the neutrino mass ordering [13]. In the case of $\delta_{CP} \neq 0$ and $\delta_{CP} \neq \pi$ there is an asymmetry due to both CP violation and matter effect. In this case it is important to discriminate between these two contributions. This would ensure to the experiment a CP violation sensitivity and the mass ordering from measurements of the total asymmetry.

The two terms can be described with a dependence on baseline and energy of the type [14]:

$$\mathcal{A}_{CP} \propto \frac{L}{E} \quad (2.1)$$

$$\mathcal{A}_{matter} \propto L \times E. \quad (2.2)$$

These asymmetries have been calculated for different baselines at both the first and second oscillation maxima.

The maximum CP asymmetry is larger than the matter one at the first oscillation maximum only for baselines less than ~ 1000 km. This could yield ambiguous results for short baselines if the hierarchy is unknown. Therefore at short baselines, any observed asymmetry could be due to either the matter effect or CP violation at the first oscillation maximum. The second maximum could represent a solution because the CP asymmetry dominates the matter one at it. Unfortunately at short baselines it occurs at an energy that isn't observable. A longer baseline is clearly needed to solve the ambiguity and make the matter asymmetry more significant. With this improvement, it would be possible to use the information from the second oscillation maximum.

In Figure 2.2, are reported the oscillation probability asymmetries as a function of δ_{CP} for different baselines. In the first row it is shown how the value of δ_{CP} is ambiguous if the mass ordering is not known. In the second row, at very long baselines, the matter asymmetry exceeds the maximal CP asymmetry at the first oscillation node. This ensures no degeneracies and the mass ordering and phase value can be resolved within the same experiment.

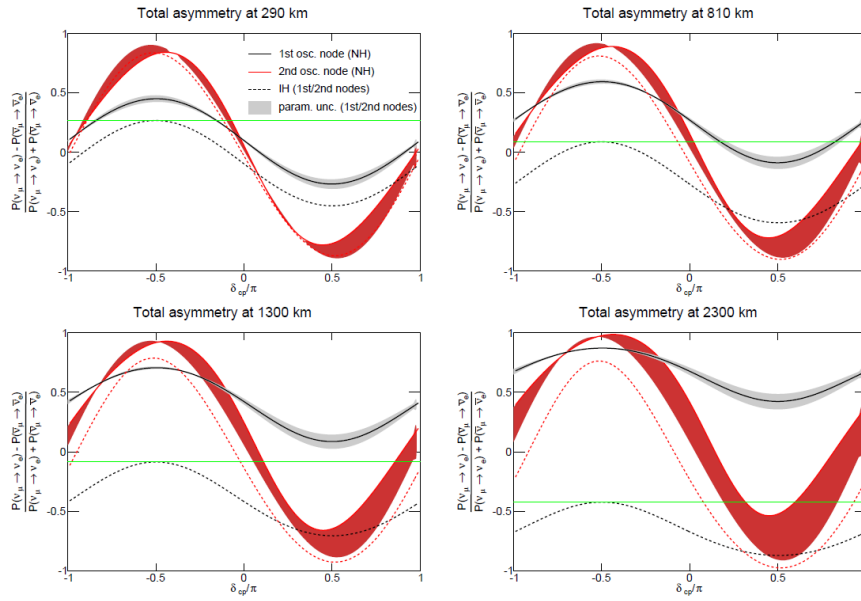


Figure 2.2: Oscillation probability asymmetries as a function of δ_{CP} for different baselines, at the first two oscillation nodes. The black line represents the total asymmetry for normal hierarchy (solid line) and inverted hierarchy (dashed line) at the first node. The red lines are the asymmetries at the second oscillation node. The green lines indicate the asymmetry at the first node for maximal CP violation ($\delta = \pi/2$) with an inverted hierarchy. It is clear how at long baselines the ambiguity is resolved [14].

With its baseline of ~ 1300 km, DUNE will be able to perform unambiguous measurements of both the mass ordering and δ_{CP} . At this baseline the asymmetry is approximately $\pm 40\%$, which exceeds the maximum possible value for the asymmetry associated with δ_{CP} .

2.3 Near detector physics

Neutrino oscillation experiments as DUNE make use of the near-far detector configuration to constrain systematic errors and mitigate their effects. The Near Detector (ND) will mainly serve as an experiment's control. It will provide a characterization of the energy spectra, along with the nature of the beam composition before oscillations. The ND therefore plays a crucial role in predicting what the oscillation signal spectrum should look like in the FD because the expected spectra are evaluated basing on the precisely measured spectra for neutrino and antineutrinos interactions in the ND. The unoscillated energy spectrum will be measured for all neutrino species in the beam ($\nu_\mu, \nu_e, \bar{\nu}_\mu$ and $\bar{\nu}_e$), along with their relative abundances. These measurements will be performed through the observation of Charged Current (CC) neutrino interactions at the ND site. The interaction rate at source will then be compared to the rate at the Far Detector. This process needs to account for different aspects which can effect the comparison. Firstly, there is a large difference between the angular acceptance of the two detectors. This makes the beam spectrum observed at the far site different from that measured at the source from the ND. Secondly, if the power beam is high, it could creates large rates at the near site implying pile-up effects compromising the detector efficiency. It is therefore necessary to evaluate with attention the technology to be chosen for the Near Detector, avoiding those with intrinsic slow response or those difficult to be operated with high pile-up rates.

The Near Detector site will also have a physics program independent from the Far Detector. It foresees deepening the study of neutrino interactions along with investigate Physics Beyond the Standard Model as non-standard interactions, sterile neutrinos or other exotic particles.

2.4 Far detector physics

2.4.1 Neutrino interactions

Main purpose of the Far Detector will be searching for ν_e appearance and ν_μ disappearance in the incoming, likely oscillated, neutrino beam.

In order to do this, it will observe the topology of neutrino interactions inside the detector volume. The most likely neutrino interactions that can occur in DUNE Far Detector are listed here below:

- Elastic Scattering (ES):

$$\text{CC : } \nu_e + e^- \rightarrow \nu_e + e^-; \quad (2.3)$$

$$\text{NC : } \nu_{\mu,\tau} + e^- \rightarrow \nu_{\mu,\tau} + e^-; \quad (2.4)$$

this reaction presents a higher cross section in the case of electronic neutrinos compared to the other two neutrino flavours.

- Quasi Elastic scattering (QE):

$$\text{CC : } \nu_e(\bar{\nu}_e) + n(p) \rightarrow e^-(e^+) + p(n); \quad (2.5)$$

$$\text{CC : } \nu_\mu(\bar{\nu}_\mu) + n(p) \rightarrow \mu^-(\mu^+) + p(n); \quad (2.6)$$

$$\text{CC : } \nu_\tau(\bar{\nu}_\tau) + n(p) \rightarrow \tau^-(\tau^+) + p(n); \quad (2.7)$$

- Non-Elastic Scattering:

$$\text{CC : } \nu_\mu + n \rightarrow p + \mu + \pi^0; \quad (2.8)$$

the π^0 can then decay in two photons (2γ).

2.4.2 Atmospheric neutrinos

In addition to the search for Super Nova Burst and proton decay, already mentioned in sec. 2.1, a large underground detector as the DUNE Far Detector would have a great potential in studying atmospheric neutrinos. Thanks to its location at a depth of ~ 1.5 km, it presents a good shielding for cosmic-ray background avoiding the use of a veto and exploiting the full fiducial mass of the detector. The Far Detector would represent a unique site to observe atmospheric neutrino interactions with excellent energy and path-length resolutions, enabling to reconstruct their momentum. This would provide high-resolution measurement of L/E , good sensitivity to mass ordering and to the octant of θ_{23} .

The sensitivity of the DUNE Far detector to atmospheric neutrino oscillation parameters has been obtained using the Monte Carlo frameworks already developed for the MINOS experiment. The geometry of a toy detector has been simulated along with the possible atmospheric neutrino interactions. The events, as usual for experiments of this kind (e.g.

Super-Kamiokande), have been classified through their vertex topology: Fully Contained (FC) or Partially Contained (PC). Events with interaction vertices outside the detector volume have not been considered.

Atmospheric neutrinos are subjected to the MSW effect when interacting with matter. This influence enhances in the few-GeV energy range for electron neutrinos at large zenith angles. This enhancement occurs for neutrinos in the normal ordering and antineutrinos in the inverted ordering. The power to resolve the mass ordering with atmospheric neutrinos comes from the observation of this effect. The mass ordering sensitivity can be greatly enhanced if neutrino and antineutrino events can be separated. A way to make this is to magnetize the detector which will not be applied to the DUNE Far Detector. Indeed, its high-resolution imaging offers possibilities for tagging features of events that provide statistical discrimination between neutrinos and antineutrinos. The two tags included for the sensitivity calculations are: a proton tag and a decay electron tag. Protons occur preferentially in neutrino interactions while decay electrons are assumed to occur 100% of the time for μ^+ and 25% of the time for μ^- .

The measurements of atmospheric neutrinos will be conducted both with and without the neutrino beam. The atmospheric neutrinos sensitivity to the mass ordering is almost independent on the CP-violating phase and strongly dependent on the true value of $\sin^2 \theta_{23}$. This independence could help in solving the degeneracies present in beam analyses.

2.5 Neutrino beam

Neutrino beams are created through interactions of other particles. As already described in section 2.3, the beam takes its origin from accelerated protons. These highly energetic protons impact on a solid target and produce mesons, mostly pions and kaons. The charged pions (π^\pm) are then focused using magnetic horns to a decay tunnel. Decaying, they produce muons ($\pi^+ \rightarrow \mu^+ + \nu_\mu$, $\pi^- \rightarrow \mu^- + \bar{\nu}_\mu$) which create neutrinos in the end ($\mu^+ \rightarrow e^+ + \nu_\mu + \nu_e$, $\mu^- \rightarrow e^- + \nu_\mu + \bar{\nu}_e$). At the end of the tunnel, the remaining muons are stopped by a muon absorber leaving only neutrinos. The nature of the beam, whether made of neutrinos or antineutrinos, can be determined by selecting the initial charged pions, through magnetic field. For its physics program, DUNE will use a beam of muonic neutrinos from accelerated protons of energy between 60-120 GeV. However, considering the nature of the decays involved, a portion of electron neutrinos will be present. Purpose of the Near Detector will be also to characterize the beam composition at this stage. The beam

will be then directed to the Far Detector to measure again the flavour composition after the oscillation.

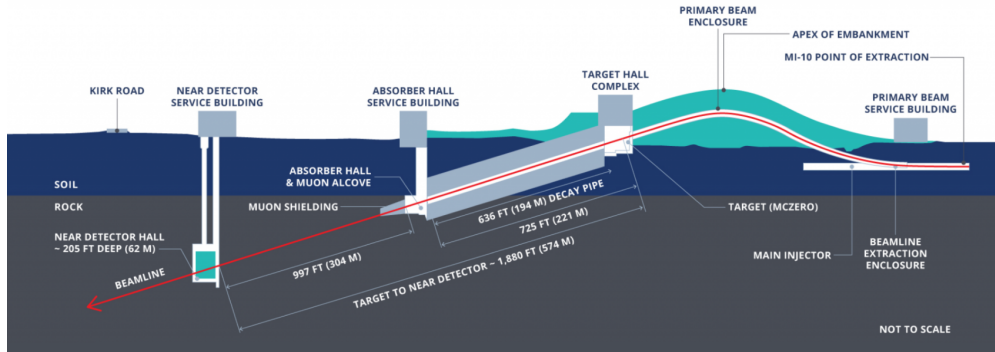


Figure 2.3: Scheme of the beam production at the Near site.

2.6 The Near Detector complex

As already said in section 2.3, the Near Detector complex will play a crucial role in the DUNE physics program. The Near Detector hall will be located underground at a distance of 574 m from the beam target. Instead of using only one detector, the complex will include three different primary detectors components. Two of them will be able to move off-axis (Fig.2.4) to study different neutrino energy spectra, while the other one will remain in a fixed on-axis position. The current design for the complex includes (Fig.2.5):

- a liquid Argon TPC (ArgonCube);
- a multi-purpose Detector (MPD) composed of a high-pressure gaseous argon TPC (HPgTPC) within a magnet surrounded by an electromagnetic calorimeter (ECALs);
- an on-axis beam monitor called System for on-Axis Neutrino Detection (SAND).

ArgonCube will have the same target nucleus of the FD in order to reduce cross section and detector systematic uncertainties for oscillation analyses. It will share also some aspects of form and functionality with it. However, some differences are necessary due to the higher beam intensity at the Near site. The intense neutrino flux and high event rate makes traditional

2.6. The Near Detector complex

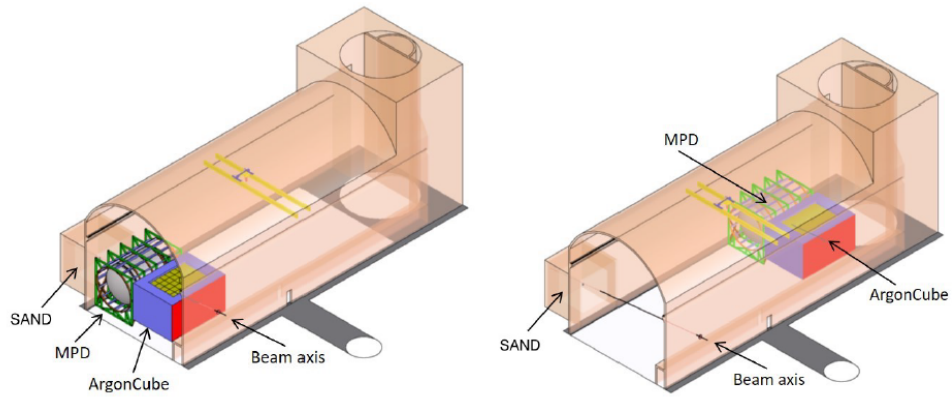


Figure 2.4: Near Detector hall. On-axis position for all the detectors (left), off-axis position for the movable components (right).

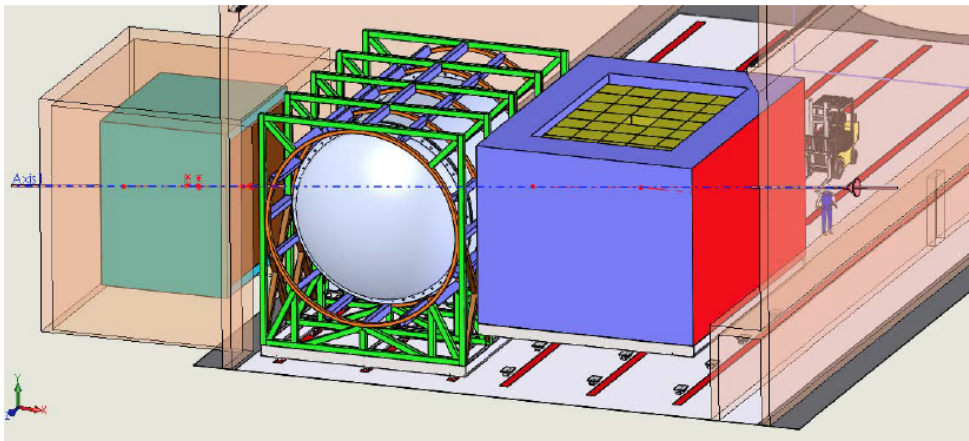


Figure 2.5: Design of the Near Detector complex. From right to left are shown: the ArgonCube TPC, the multi-purpose Detector (MPD) and the System for on-Axis Neutrino Detection (SAND).

TPCs unsuitable. ArgonCube is the result of a program of research and development for a new LAr TPC design [17][18]. In order to improve drift field stability, it will use a detector modularization by reducing high voltage and LAr purity requirements. The three dimensions reconstruction of particle interactions will be simplified by pixelized charge readout. To increase the light yield, a new dielectric light detection techniques will be used improving the localization of light signals.

The multipurpose detector (MPD) will be used to extend and enhance the capabilities of ArgonCube. To determine neutrino energy, the muon momentum is a fundamental component to know. However, for muons with energy above ~ 0.7 GeV/c the acceptance of the LArTPC begins to decrease due to the lack of containment. This makes necessary the use of a magnetic spectrometer downstream ArgonCube, to measure the charge sign and momentum of these muons exiting the previous detector.

ArgonCube and MPD will be able to change position moving off the beam axis. Measurements taken in an off-axis position allow to investigate the incident neutrino flux spectrum in a different way, as the spectrum becomes somewhat monochromatic with the mean energy dropping. Changing position at different off-axis angles, enables to deepen the study of the neutrino flux and interaction cross section along with better understand the response of the detector.

To ensure a comparison and a systematic cross-check of the neutrino flux determination performed by the first detectors system, a second one located on-axis is adopted. The System for on-Axis Neutrino Detection (SAND), will be composed of a three dimensions scintillator tracker, inside a TPC and an Electronic Calorimeter (ECAL). The system will be surrounded by a magnet. Because the Far Detector (FD) will be located on-axis, the study of the spectrum at this position is of fundamental importance in order to model and use it to extract the oscillation parameters at the FD.

2.7 The Far Detector

To fulfill its physics program (section 2.1), DUNE will make use of a massive detector able to observe rare events as neutrino interactions, with a sub-centimeter spatial resolution. It will enable to identify the signatures of the physics processes and to distinguish them among background events.

In order to study a possible CP violation, aim of the experiment is to study the appearance of a ν_e component in the ν_μ beam after the oscillation. To make this possible, it is necessary for the detector the ability to

distinguish electromagnetic showers induced by charged current ν_e interactions, from those arising from other events as photons emitted from the π^0 decay. Photon-induced showers can be identified by their topology and dE/dx in the process. Differently from electron-induced showers, photon-induced ones present a gap prior to conversion and a higher dE/dx at the beginning of the avalanche, which makes possible to solve the ambiguity.

The search for nucleon decay will be conducted mainly in the decay channel $p \rightarrow K^+\bar{\nu}$, needing a precision of few centimeters in the kaon tracks identification. A fundamental task in this study is to fiducialize this nucleon-decay events in order to distinguish them from the cosmic-muon-induced ones, which represent a background source. The necessity of a photon detection system able to observe the Argon scintillation light emitted in the process becomes fundamental to determine the time of the event.

Studying Supernova Neutrino Bursts (SNB) implies a high data rate and the necessity of keeping the detector active for long periods of time in order not to miss any of those rare events searched for. A SNB event is identified by the observation of electrons tracks spread over the entire detector volume at few centimeters in length from CC ν_e interactions and with energy of \sim MeV.

At the Sanford Underground Research Facility (SURF) a site to host and provide infrastructure for the DUNE Far Detector (FD) will be constructed. The FD will consist of four Liquid Argon Time Projection Cham-

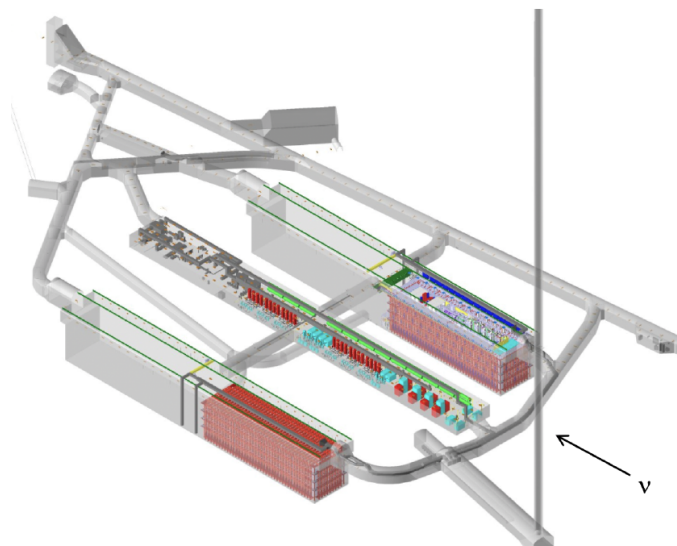


Figure 2.6: Far Detector site.

ber (LArTPC) detector modules. They will be installed at a depth of ~ 1.5 km and have a fiducial mass at least of 10 kt (Fig.2.6). Each LArTPC will be inserted in a cryostat module filled with Liquid Argon and serves as a target for the neutrino interactions.

The design of the first two LArTPC modules will use the Single Phase technology. A Dual Phase technology is expected to be used for the others. To test both the SP and DP technologies, two prototype detectors have been constructed at CERN. The ProtoDUNE-SP and ProtoDUNE-DP are reduced in size but use the same components to those of the future modules. Tests conducted with hadron beam and cosmic rays have demonstrated the excellent performances of the detectors.

2.7.1 Single Phase Liquid Argon Time Projection Chamber (SP TPC)

Charged particles produced by neutrino interactions in liquid argon induce scintillation and ionization. In a Single Phase Time Projection Chamber (SP TPC), ionization electrons are drifted up through the detector volume under the influence of an electric field towards the anode, where they are read out (Fig.2.7). The process develops on a time scale of the milliseconds.

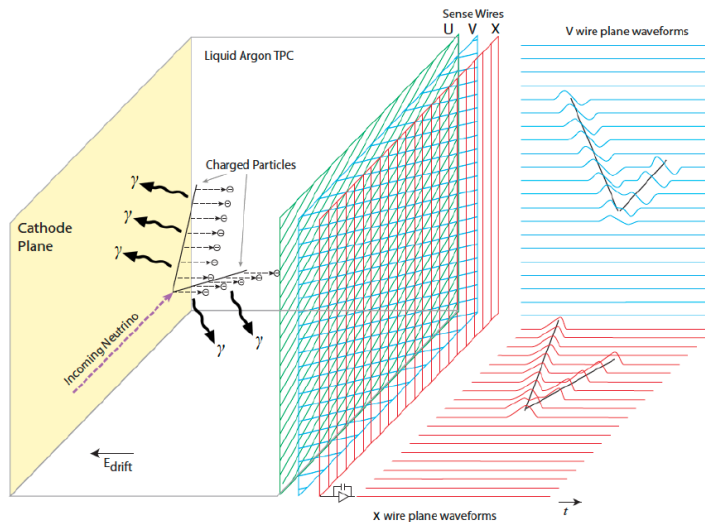


Figure 2.7: Neutrino interaction in a Single Phase LArTPC.

The DUNE's SP LArTPC module will be instrumented with two cathode planes and three anode planes (Fig.2.8) [20].

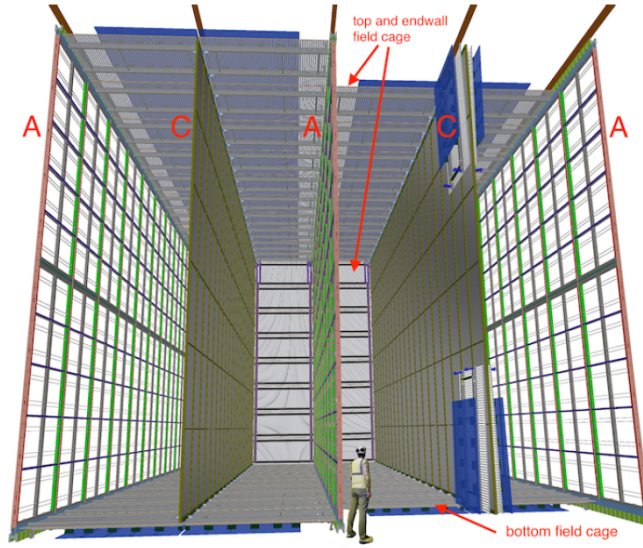


Figure 2.8: Scheme for the DUNE's SP LArTPC: anode (A) and cathode (C) walls

The design for the anode wall consists of three planes of active wires, two faces each, plus an additional shielding grid layer around them. The first two layers produce bipolar induction signals and the final one collects the drifting electrons, producing a monopolar signal. The unit element of the Anode wall is the Anode Planes Assembly (APA) (Fig.2.10) and each wall has a total of 50 Anode Planes Assemblies (APA) stacked two by two (Fig.2.9). At the top end and bottom end of each top APA, the front end readout electronic is attached (Cold Electronics, CE). By placing the electronics in LAr, there is a reduction in the thermal noise. Inside the APA the Photon Detection (PD) system is installed by means of slots (Fig.2.9).

The topology of neutrino interaction vertex is reconstructed in the SP LArTPC: two of the three spatial coordinates (y and z) are established from the position of the fired wires in the APA, while the third one is obtained by the arrival time of the charge. The t_0 of the event is given by the scintillation light produced by the LAr excitation and collected by the PD system. Through their time difference and knowing the drift velocity, it is possible to calculate the position. The charged lepton produced in a CC neutrino interaction is identify by analyzing the reconstructed topology of the event. The flavour identification of the neutrino immediately occurs through this pattern recognition of the event.

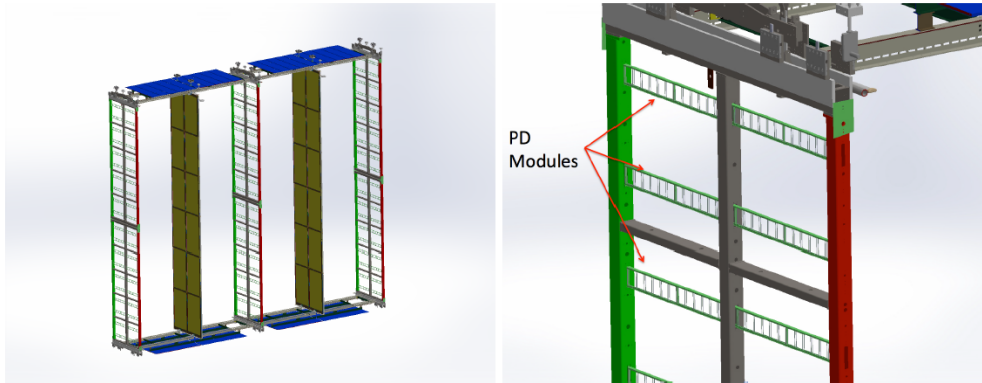


Figure 2.9: Left: section of a the anode and cathode walls where the two anode APAs stacked together are visible. Right: Photon Detection modules inserted inside an APA.

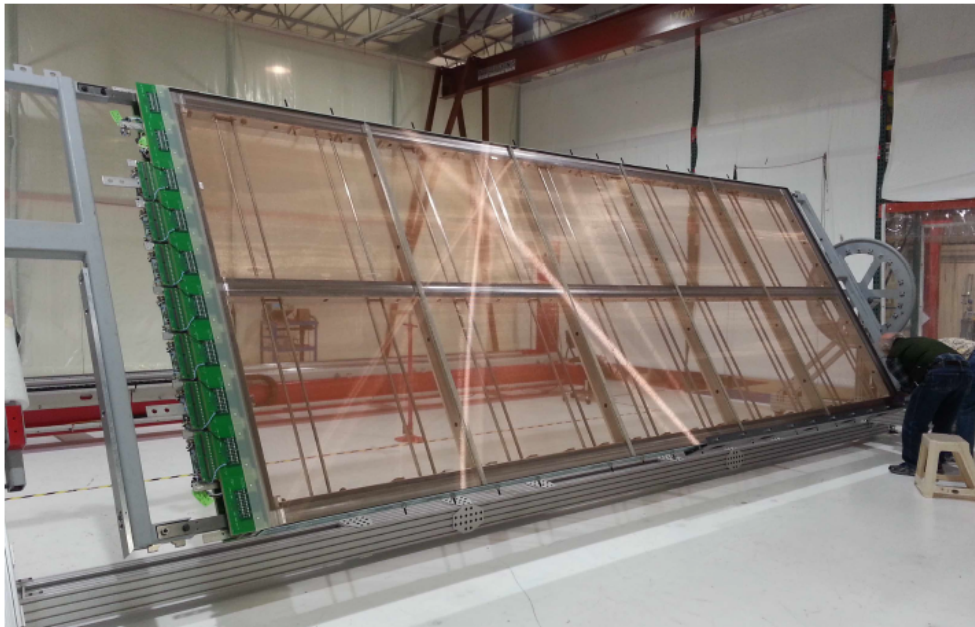


Figure 2.10: A single completed APA for the ProtoDUNE-SP.

2.7.2 Photon detection system

The main task of the Photon Detection system (PD) is to collect and measure the scintillation light emitted during the interaction process. One of the problems to face in the realization of this objective, is the necessity to reduce the impact of the PD system on the active volume of LAr while maximizing the light collection efficiency. This makes impossible the use of the traditional large area photomultiplier tubes (PMT). For the PD system of the DUNE Far Detector, the solution adopted will be to select sensors with small surface but high efficiency and mounting them inside the inactive space of the Anode Plane Assemblies structure. This will reduce to zero the impact of the PD system on the active volume.

The process which leads to the collection of scintillation light over a large area in a compact space is composed of different steps. First of all, the scintillation photons emitted by the LAr de-excitation are Vacuum-Ultra-Violet (VUV) photons with $\lambda \sim 127$ nm, which implies the necessity of a conversion to a longer wavelength to which the photosensors are sensitive. This conversion occurs inside the light collector elements composing each PD module. The photons are then directed, as efficiently as possible, to photosensors able to convert the collected charge into electrical signal. Traditional photomultiplier will not be used because of space constraints reasons, while Silicon Photomultipliers (SiPM) will be the best choice for the DUNE's PD system thanks to their dimensions of few millimeters.

The specific design for the PD light collector module, is called X-ARAPUCA [16]. It consists of cells which act as light trap and captures photons inside boxes with highly reflective internal surfaces. The photons are then collected by Silicon Photomultipliers (SiPMs) located on the long side of each PD module.

An X-ARAPUCA cell, is composed of different layers (Fig.2.11). The incoming photon firstly impacts on a first layer of wavelength-shifting (WLS) material (p-terphenyl, PTP) covering a dichroic filter plate which acts as a light trap, capturing the photon inside the volume of the cell. In the innermost part of the box, a WLS plate acting as a light guide transports the photon to the readout via total internal reflection. This configuration minimizes the number of reflections inside the cell and thus the photon loss probability which means an increase in the collection efficiency.

A PD module is composed of four X-ARAPUCA supercells (Fig.2.12), each formed by an array of six dichroic filters forming the entrance window, behind which the WLS plate is located (Fig.2.13). The PD modules installed in the side APAs are required to collect light only from one side,

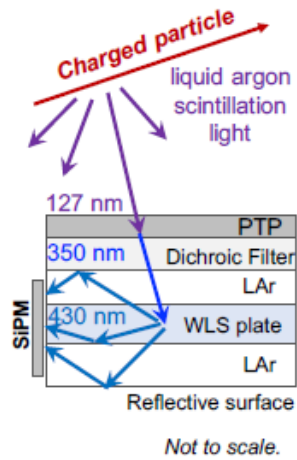


Figure 2.11: Scheme of the different layers of an X-ARAPUCA cell.

while those in the central APAs from both sides.

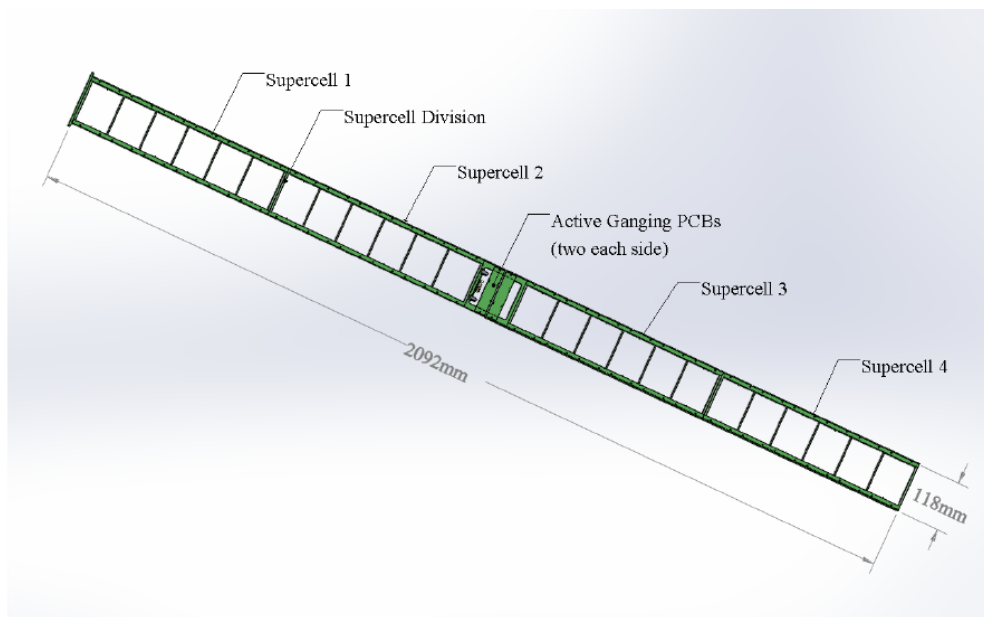


Figure 2.12: Single photon detection frame containing 4 X-ARAPUCA supercells. The SiPMs are mounted to PCBs, called “photosensor mounting boards”, located on the long side of each PD module.

In both cases, the SiPMs arrays are installed on two of the narrow sides of the cell perpendicular to the windows and placed symmetrically with respect to the light guide plane. Half of the active area of the sensor

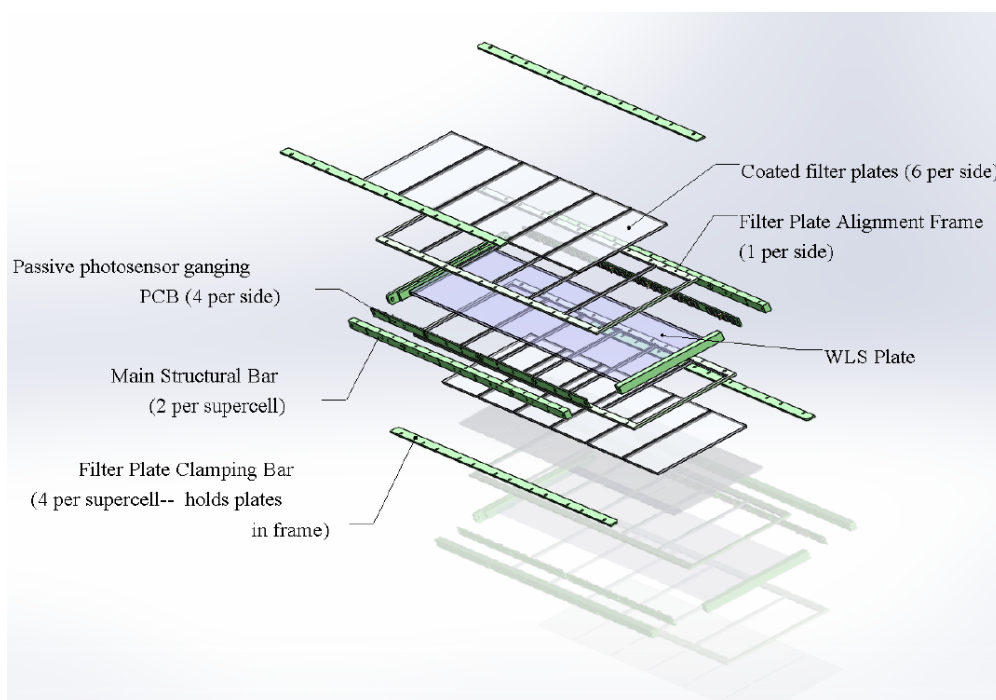


Figure 2.13: A detailed exploded view of an X-ARAPUCA supercell.

is able to collect photons coming from the WLS plate, while the other half, one quarter on either side of the plate, is dedicated to the collection of the photons reflected off the other part of the cell. The total area of the SiPMs will be of $6 \times 6 \text{ mm}^2$.

The SiPMs are mounted in groups of six to PCBs called "photosensor mounting boards" (Fig.2.14), each supercell uses eight of them for a total number of 48 SiPMs per supercell and 192 SiPMs per PD module. The sensors on a same photosensor board are electrically connected in parallel ("passively ganged") to reduce the number of readout channels.

The eight passively ganged signals from each supercell are actively ganged into only one output channel resulting in a total number of four channel per PD module. The total number of SiPMs which will be used for the Far Detector PD system will be of the order of ~ 300000 . These sensors will work in a cryogenic environment being immersed in Liquid Argon. This requires to ensure their mechanical and electrical integrity in such an extreme working condition. Currently, two different vendors are engaged in the realization of new technologies for these devices: the Hamamatsu Photonics K.K. (HBK) and the Italian Fondazione Bruno Kessler (FBK).

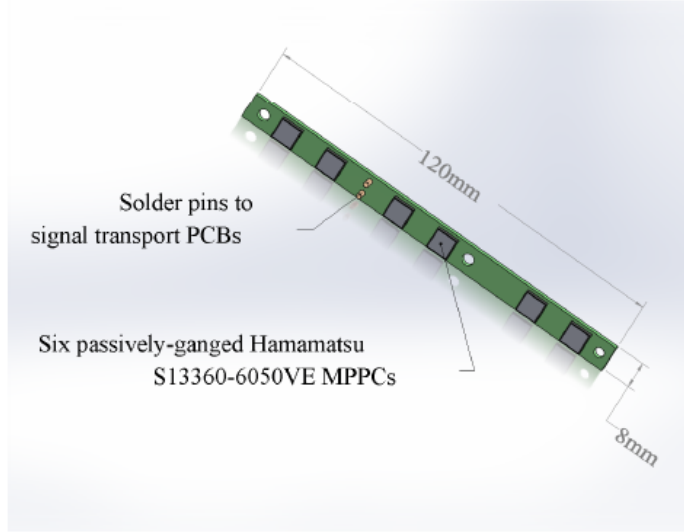


Figure 2.14: Design of a Photosensor Mounting Board (PMB) for a Photon Detection module. Six SiPMs are passively ganged and the resulting ganged signals are transmitted to the active ganging circuits.

2.7.3 Liquid Argon

The Liquid Argon filling the detector module represents the target nucleus for neutrino interactions. An Argon atom can undergo two different phenomena: ionization and excitation (Fig.2.15). From the first case, an electron-positive ion pair is formed producing the drifting electron travelling towards the anode wall. In the second one, scintillation light is emitted following the de-excitation of the singlet and triplet excited states ($^1\Sigma, ^3\Sigma$) to the ground state. The characteristic time for the de-excitation in the two cases is different, with a fast component $\tau_{fast} \simeq 6$ ns in the first one and a slow component of $\tau_{slow} \simeq 1.5 \mu s$ in the latter one. Both decays produce photons emitted in a 10 nm band centered around 127 nm referred to as Vacuum Ultra Violet (VUV) photons.

In order to take the most advantage from Liquid Argon, it is fundamental to ensure its purity. Impurities can either absorb the ionization electrons or quench the scintillation light emitted. Oxygen is an electronegative contaminant which can effect the drifting electrons by absorbing them. For this reason the requested purity from electronegative elements in Argon is <100 parts per trillions O_2 equivalent, ensuring the requirement of >3 ms ionization-electron lifetime at 500 V/cm drift voltage.

Contaminants as Nitrogen can instead quench scintillation photons emitted by charged particles produced in the interaction. In this case the

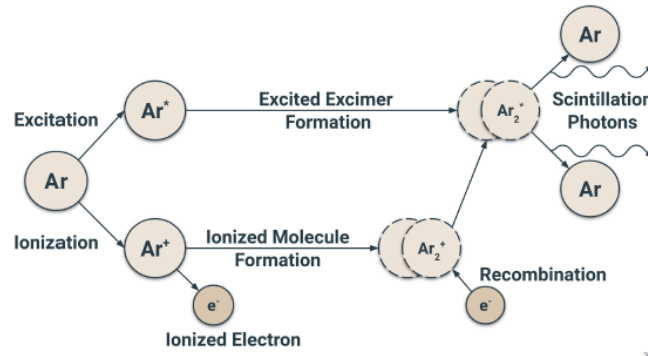


Figure 2.15: Schematic description of the scintillation light emission process in LAr.

purity requirement is <25 parts per million to ensure the detection of at least 0.5 photoelectrons per MeV for events, through the entire volume.

To satisfy these requirements, a purification system will be adopted constantly fluxing Argon through it.

2.7.4 Dual Phase Time Projection Chamber

The operating system of a Dual Phase LAr TPC is shown in Fig.2.16. This technology presents some differences to the Single Phase one. Charged particles entering the Liquid Argon volume produce ionization and scintillation light. A high electric field is applied inside the Chamber drifting the ionization products. In a Dual Phase (DP) TPC, the electrons drift vertically towards the anode reaching a layer of gas located above the liquid. In this region, a higher electric field drifts the electrons creating an avalanche and thus a proportional signal on the anode, where the charges are collected. The scintillation light emitted is then collected by photomultiplier tubes (PMTs) located underneath the cathode.

The DP technology presents some advantages as well as disadvantages. The drift length is longer compared to that of a SP LArTPC, which implies an improved signal-to-noise (S/N) ratio in the charge readout. On the other hand, it requires a higher voltage on the cathode and, extremely important, strong constraints on the Argon purity and electronic noise reduction.

2.8 DUNE Prototypes

In order to test both the Single Phase (SP) and Dual Phase (DP) technologies, two prototype detectors have been constructed at CERN.

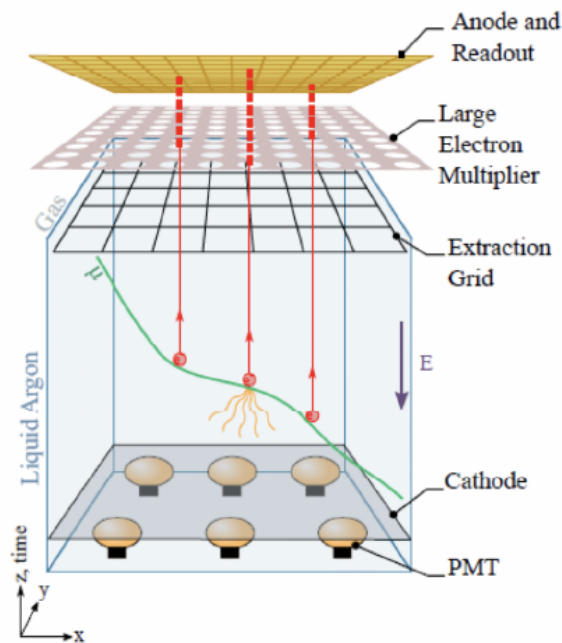


Figure 2.16: Operating system of a Dual Phase Liquid Argon Time Projection Chamber (DP LAr TPC).

The ProtoDUNE-SP and ProtoDUNE-DP are reduced in size but use the same components to those of the future module. ProtoDUNE-SP has the same maximum drift length as the planned full SP module. Goal of the prototyping program was to ensure the quality of the components used and validate the installation procedures. Test conducted with hadron beam and cosmic rays have demonstrated the excellent performances of the detectors, providing important informations on the design, calibration and simulation of the detector modules. Thanks to the data collected during the first beam run, the Photon Detection system response can be characterized.

A second beam run is planned for the future: the ProtoDUNE-SP II prototype will be improved in some aspects in order to optimize the response of the detector.

Chapter 3

Silicon Photomultipliers

3.1 Silicon photodiodes

A photodiode is a diode with a p - n junction strongly asymmetrically doped: the p side indeed presents a higher doping than the n side.

In the region between the two junctions, the majority carriers diffuse to the opposite electrodes where they are collected. Therefore an electric field between the two junction is formed opposing the charge diffusion and, if strong enough and no external bias voltage is applied, creating a steady state of equilibrium in the region. The barrier voltage created is called *built-in* voltage (V_{bi}). This region, which presents a lack of charge carriers, is known as *depletion region* (Fig.3.1). The width W of the

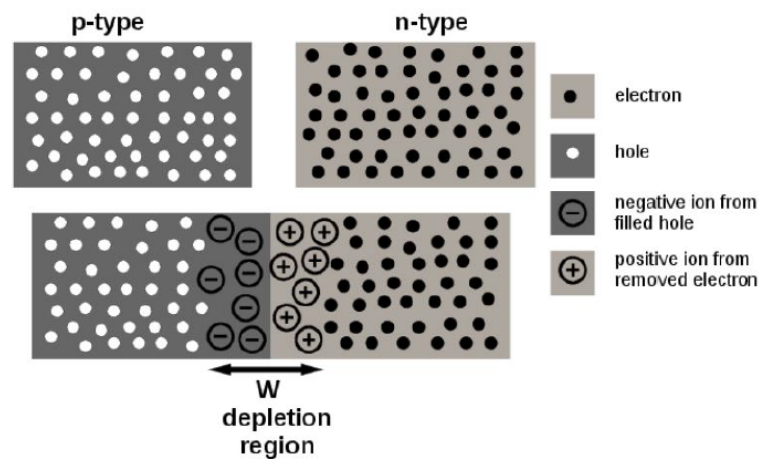


Figure 3.1: Formation of the *depletion region* in a p - n junction.

depletion region, at the thermal equilibrium, is:

$$W = \sqrt{\frac{2\epsilon_s}{q} \left[\frac{N_A + N_D}{N_A N_D} \right] V_{bi}} \quad (3.1)$$

where N_A is the number of acceptors, N_D the number of donors, ϵ_s is the semiconductor dielectric permittivity and V_{bi} the built-in potential.

Basing on the external applied voltage, these kind of diodes work in two different configurations: *forward (reverse) bias* polarization when a positive (negative) voltage is applied to the p side (Fig.3.2 (a) (b)). In the "forward case", they behave as normal diodes and a current can flow. Because the built-in electric field results opposite to the applied electric field, the total resultant field is smaller than the original built-in electric field which creates a narrower depletion region. In the "reverse case", the two electric field have the same direction resulting in a larger total field and thus creating an enlargement of the depletion region (Fig.3.2(b)).

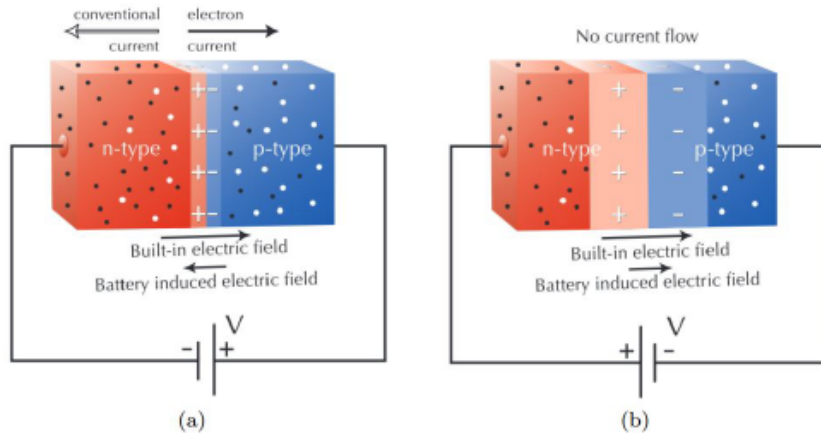


Figure 3.2: (a) Forward bias polarization for a $p-n$ junction. (b) Reverse bias polarization for a $p-n$ junction.

In a more specific description of the latter case, a small current still flows through the depletion region and eventually saturate at a small constant value (I_{sat}) but the resistance is so high that it can be neglected. The resulting current-voltage relation, known as I-V curve (Fig.3.3), gives a description of the correlation between the applied voltage and the resulting current in the junction.

In the reverse bias polarization, if the applied voltage is strong enough, the majority carriers, while diffusing, create an electron-ion pair along their path. This can start an avalanche process inside the depletion region,

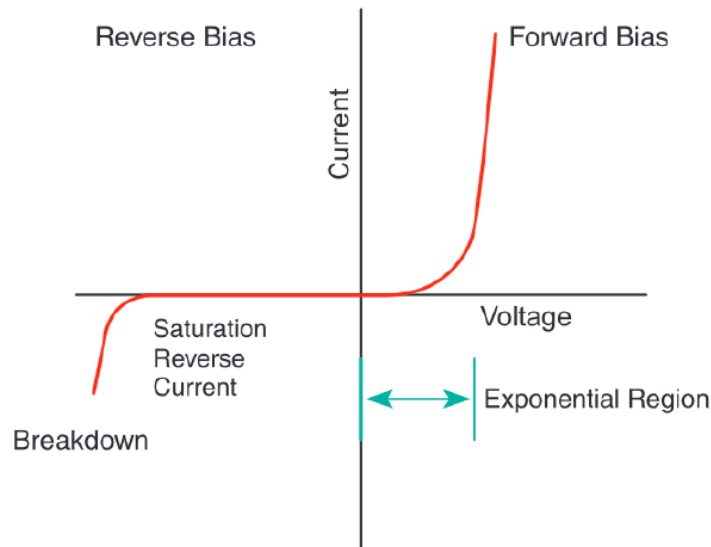


Figure 3.3: I-V curve of a p - n junction.

creating an increasing current. The critical voltage at which the avalanche occurs is known as the *break down voltage* (V_{bd}).

An impinging photon, arriving with a sufficient energy on the photodiode, can be absorbed and create an electron-ion pair. If the pair is produced inside the depletion region, the charged particles are drifted to the corresponding electrodes under the effect of the electric field and a photocurrent is created. The p - n junction thus, working at a reverse bias polarization, results suitable to be used as a photodetector. There are different types of photodetectors exploiting the mechanism described above.

The PIN photodiode is a simple device composed of a p semiconductor layer, another layer of n semiconductor and, between them, a large region of intrinsic undoped semiconductor. This design creates a wide depletion region with high uniform electric field between the two junctions. Because of it, the drifting velocity of the carriers increases and the process becomes faster making the photodiode suitable for high frequency measurements.

The Avalanche PhotoDiodes (APDs) are particular types of p - n diodes, reverse bias polarized near the breakdown voltage and working in the charge multiplication regime (*Geiger mode*). Their particular internal structures consists in four semiconductor layers, asymmetrically doped, in the following order (Fig.3.4):

- a p^+ region, heavily doped with acceptors;

- a region of intrinsic semiconductor, used to maintain the electric field approximately constant;
- a p region doped with acceptors but fewer than the previous one;
- a n^+ region, heavily doped with donors.

This particular structure creates a high electric field within the p region, which plays a fundamental role. The primary charges produced in the intrinsic region reach the p region, where they are drifted under the effect of the electric field and produce secondary charges generating an avalanche.

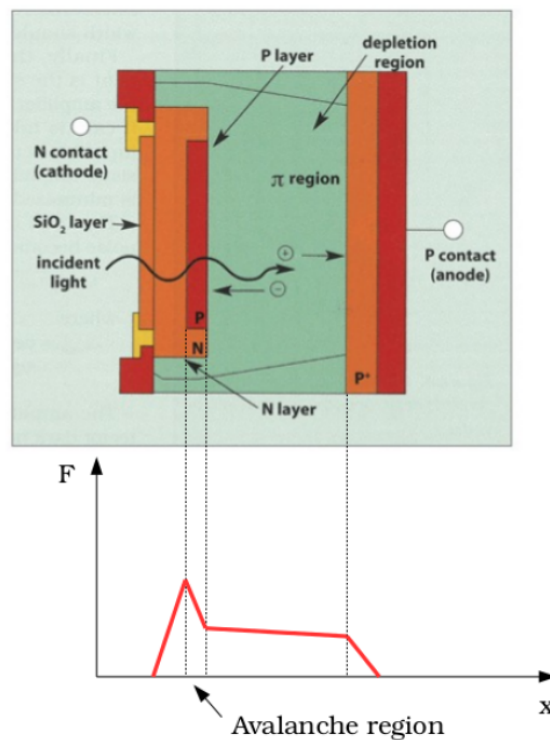


Figure 3.4: Layered structure of an Avalanche PhotoDiode (top) with the corresponding electric field F (bottom).

3.2 Silicon Photomultipliers (SiPMs)

Silicon Photomultipliers are arrays of single-photon Avalanche PhotoDiodes (APDs), arranged in parallel on a common Silicon substrate. Each

photodiodes is referred to as a *pixel* or *microcell*, working in reverse biased polarization at a voltage above the V_{bd} and thus in *Geiger* mode. If a carrier is generated by a photon or thermally inside the pixel, it can activate an avalanche confined in it. The Geiger discharge is generated when the electric field inside the depletion region is sufficiently high that the drifted carriers produce a secondary ionization along their path. The discharge is interrupted when the voltage returns below the breakdown voltage, due to a resistance coupled in series to each photodiode (*quenching* resistance). The pixel then takes a characteristic time to reach again the multiplication regime and being sensitive to another discharge. The *recovery time* (τ_{rec}) of the microcell is:

$$\tau_{rec} = R_q \cdot C \quad (3.2)$$

which is dependent on the pixel capacitance C and the quenching resistance R_q . This cycle of breakdown, avalanche, quench and reset is reported in Fig.3.5. Because each pixel works independently, only the previously

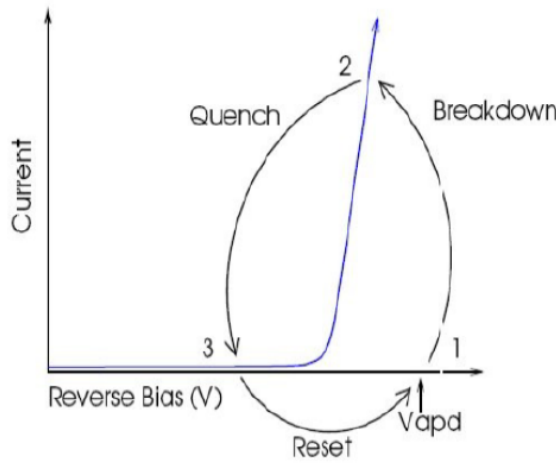


Figure 3.5: Cycle of: breakdown, avalanche, quench and reset for a SiPM working in reversed bias polarization.

fired pixel needs a reset time, while the others remain sensitive. Each microcell is connected to a common output giving a resulting signal which is the sum of the single fired pixels. The quasi-analog output obtained is a measure of the magnitude of the photon flux detected and each detected photon results in a highly quantized output pulse. Because the device works in Geiger mode, it is not possible to distinguish an avalanche

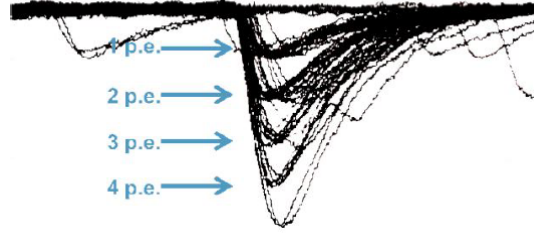


Figure 3.6: Output signal of a SiPM view through an oscilloscope. The quantized pulse correspond to different numbers of detected photoelectrons.

formed by a single photon from that produced by more photons simultaneously impinging on the same cell. The SiPM thus works linearly in a dynamic range from the lowest detectable signal, to a limit at which all the microcells are detecting photons simultaneously. Beyond this limit, the output signal saturates since no more pixels are available to detect incoming photons until some of them recovered back to their sensitive state. Thus, due to the finite number of cells, deviations from linearity occur when the number of photons is comparable to the number of available pixels. The dynamic range depends on the number of cells composing the SiPM and of its PDE. The number of fired cells N_{fired} is:

$$N_{fired} = N_{tot} \left[1 - \exp\left(\frac{-N_{ph} \cdot PDE}{N_{tot}}\right) \right] \quad (3.3)$$

where N_{tot} is the number of SiPM pixels and N_{ph} the total number of incoming photons.

The Photon Detection Efficiency (PDE) of a SiPM is:

$$PDE = QE \cdot \epsilon_G \cdot A_{pixels}/A_{total} \quad (3.4)$$

where: QE is the *Quantum Efficiency*, i.e. the probability that a photon impinging on the SiPM is transmitted in the Silicon and finally converted in an electron-hole pair, A_{pixels}/A_{total} is the geometric efficiency (*fill factor*) or the fraction of total area occupied by the active pixels and ϵ_G , the probability that an electron-hole pair successfully imitates an avalanche process inside the pixel.

The gain G of a single pixel grows linearly with the over-voltage at which it operates ($\Delta V_{ov} = V_{bias} - V_{br}$):

$$G = \frac{C \Delta V_{ov}}{q} \quad (3.5)$$

where C is the microcell capacitance and q the electron charge. The total gain thus is the ratio between the collected charge and the electron charge. The typical gain of a SiPM is of the order of $\sim 10^6$ electrons for a single photoelectron produced [21].

The main advantages of SiPMs are:

- insensitivity to magnetic fields, unlike the traditional photomultiplier tubes (PMT) usually used for application in High Energy Physics;
- low operating voltages, usually of the order of $\sim 50\text{V}$;
- small size thanks to their compact design;
- robust photon conversion efficiency with a sensitivity to single photoelectrons;
- high gain ($\sim 10^6$), similar to that of PMT but with a reduced surface.

3.3 Noise sources in SiPMs

Due to the very high gain of SiPMs ($\sim 10^6$), their electronic noise is negligibly small compared to standard APDs, where G is typically ~ 100 . In SiPMs, the level of electronic noise corresponds to less than 10% of the signal given by photoelectron [23]. The main noise source is the dark current; other sources are optical crosstalk and afterpulses.

3.3.1 Dark current

The *dark current* arises from charge carriers thermally originated in the sensitive volume which, under the effect of the high electric field, trigger an avalanche in absence of light. The correspondent resulting signal is identical to that produced by a photoelectron, creating thus a noise source at the single photon level.

The probability of thermally producing electron-hole pairs describes the dependency of the *Dark Count Rate* (DCR) from the temperature:

$$P(T) = CT^{3/2}\exp(-E_g/2k_B T) \quad (3.6)$$

where T is the absolute temperature, E_g the bandgap energy, k_b the Boltzmann constant and C a proportionality constant. While the effect of the DCR can be neglected for measurements of high amplitude signals, it can significantly affect the detection of very small light signals of one or few

photoelectrons. This can limit the performances of the devices at room temperature at which the dark count rate is $\sim 100\text{kHz}/\text{mm}^2$. The effect can be partially reduced by operating at lower temperatures (at 100 K the DCR is $200\text{Hz}/\text{mm}^2$) or decreasing the volume of the depletion region. The DCR can be substantially reduced by increasing the threshold of the readout electronics to value larger than the amplitude of the single photoelectron signal. To characterize the DCR of a SiPM, a threshold scan can be performed increasing the threshold at different overvoltage. The curves obtained are called *staircase curves* (Fig.3.7).

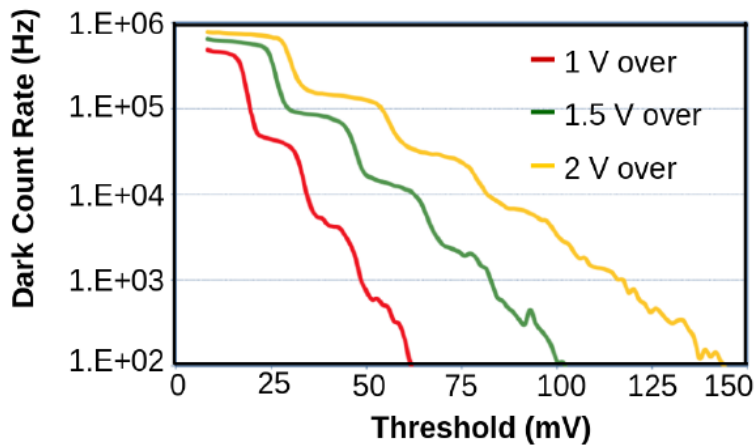


Figure 3.7: *Staircase curves*: dark count rate as a function of counting threshold for different over-voltages.

The presence in the dark count events of signals with amplitude larger than the single photoelectron is due to the *optical crosstalk*.

3.3.2 Crosstalk

Although the pixels of a SiPM are design to work individually, the *optical crosstalk* can introduce an inter-pixel coupling. This phenomenon, which represents a noise source, originates from photons emitted by accelerated electrons during a Geiger discharge inside a pixel, which can migrate to the neighbouring cells and trigger a second avalanche (Fig.3.8). Typically there is a rate of $\sim 10^{-5}$ photons emitted per electrons. The photons emitted with λ between 850-1100 nm are particular critical. Photons with a smaller wavelength are absorbed by the pixel from which they are originated, but those with a larger λ can travel for longer distance without being absorbed.

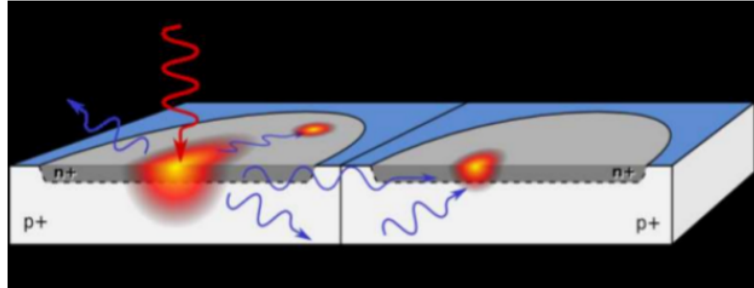


Figure 3.8: Sketch of the optical crosstalk phenomenon, between two adjacent microcells.

Optical crosstalk leads to a non-Poissonian behaviour of the distribution of the number of fired pixels. The process is instantaneous and thus single photons can generate signals equivalent to a 2 or more photoelectron event.

The crosstalk probability is defined as the probability that a fired microcell initiates an avalanche in another microcells. It is a function of the SiPM overvoltage and the distance between the adjacent microcells. The probability can be estimated as the ratio between the count rate at the second photoelectron level and the count rate at the single photoelectron level.

There are different ways to reduce the optical crosstalk phenomenon, for example: i) increasing the distance between the pixels, ii) introducing trenches acting as optical insulators, or iii) lowering the bias in order to reduce the probability of triggering an avalanche and thus the crosstalk effects. Some of these solution have disadvantages: the first one reduces the optical crosstalk at the expense of the geometrical fill factor and, along with the latter one, lowers the PDE. The second solution is the most convenient and used one in the SiPM production.

3.3.3 Afterpulsing

During the discharge process, the charge carriers can be trapped by impurities inside the Silicon crystal lattice and released after a characteristic time of the material. This phenomenon, known as *afterpulsing*, can then trigger a new avalanche after the breakdown. The delayed resulting pulse simulates a single photoelectron signal and decreases the photon counting resolution (Fig.3.9). If the release takes place during the recovery time of the microcell, it provides a contribution to the integrated output

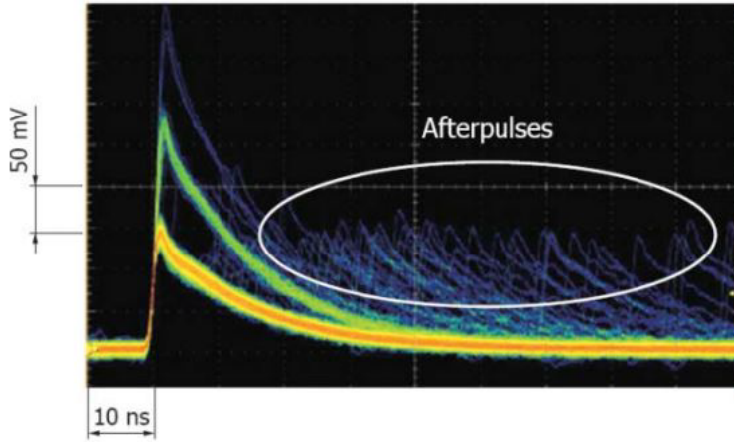


Figure 3.9: Afterpulse signals seen at the oscilloscope.

signal altering the measure of the collected charge. If instead the time delay is larger than the pixel recovery time, a standard avalanche signal is triggered.

The afterpulsing probability increases with the amount of charge flowing through the diode during the discharge. Thus, it grows with the increasing bias polarization.

3.4 SiPMs features at cryogenic temperature

In recent years in several big scientific experiments, there has been a growing interest in considering SiPMs for the readout of liquid noble-gases scintillators, such as Liquid Xenon (LXe) and Liquid Argon (LAr), as a replacement for the more traditional PMTs. Such applications usually require that the detectors are operated at cryogenic temperature, at which the SiPMs must operate successfully and with good performance.

In order to characterize the devices for this kind of applications, several studies have analyzed the main features of the sensors at cryogenic temperature. In this paragraph the description of their temperature dependence is reported.

One of the results for SiPMs working in a cryogenic environment is the reduction of the breakdown voltage. At low temperatures, the mean free path between scattering of carriers that drift in the high-field region increases. This implies an increasing in the acceleration of the carriers at a given electric field and, thus, breakdown can be achieved at a lower bias. A lower value of the breakdown voltage influences the gain and PDE

of the devices because of the different depletion of the pixel at different temperatures at a given overvoltage.

The quenching resistor of the SiPMs is usually made of polysilicon which, unlike metal resistors, presents a large thermal coefficient. Therefore, its value also undergoes significant variations with temperature. An increasing of the quenching resistor is expected at cryogenic temperature. This consequently increases the recharge time constant of the SiPMs microcells, affecting the afterpulses effects as it will be described later on.

An important aspect to consider, operating the SiPMs at low temperature, is the effect on the different noise sources. At temperature between $200 \text{ K} < T < 300 \text{ K}$ the Dark Count Rate (DCR) is dominated by field-enhanced thermal generation. Lowering the temperature below $\sim 200 \text{ K}$ DCR is dominated by direct, band-to-band tunneling which is weaker dependent on T . Reaching cryogenic temperature (below 80 K) the DCR can assume value of the order of few mHz/mm^2 . A possible explanation for this behaviour could be additional carrier losses due to ionized impurities acting as shallow traps.

The Crosstalk (CT) results being weakly dependent on temperature. This could be explained with the fact that the emission of secondary photons by avalanche does not undergo major changes with cooling. The dependence of CT probability on temperature can thus be related to changes in gain and PDE related to a decrease of the V_{BD} already mentioned.

Afterpulsing probability manifests a very different behaviour on temperature. As reported from some studies [24], below 150 K it starts rapidly rising as T further decreases. Because the phenomenon is related to carrier trapping during avalanches, this behaviour could be attributed to a longer emission time constant at cryogenic temperature by new trapping centers becoming active. This effect needs to be considered along with the competing effect on the quenching resistor, already mentioned.

Chapter 4

SiPMs characterization

This chapter describes the experimental test campaign I conducted in order to obtain a full characterization at single-SiPM level of all samples. I participated in the development of an experimental setup suitable for the tests both at room and cryogenic temperature. A special emphasis is given on the cryo-reliability of the sensors, i.e. the stability of electric and mechanical properties after thermal cycles at room and 77 K temperature. The characterization of the SiPMs includes the study of the I-V curves, measurements of Dark Count Rate and correlated noise.

4.1 DUNE requirements

The DUNE's Far Detector Photon Detection system (PD), will be composed of light collectors coupled with Silicon Photomultipliers (sec. 2.7.2). Given the large number of light collecting systems that are going to work at cryogenic temperature, an accurate selection and characterization of the SiPMs is envisaged. The experiment has stringent accessibility and longevity constraints for installed devices (Tab.4.2).

One of the issues of working in a cryogenic environment is the change in material properties and thermal stresses induced in the device packaging due to differential coefficients of thermal expansion (CTEs). This critical aspect needs to be investigated in order to ensure the long-term reliability of the photosensors through several thermal cycles. The sensors fulfill the DUNE specifications if they stand >20 thermal cycles.

Another requirement set by the experiment is a limited number of readout channels. For this reason, the SiPMs will be mounted in group of six on a same photosensors board and electrically connected in parallel (*passively ganged*), each having the same voltage to them. To ensure a

Low level specifications	Value
Max nominal operating Voltage	50 V at cold
Dark Count Rate (DCR)	<100 mHz/mm ²
Correlated noise	<35%
Time resolution	<20 μ s
Recovery time	$\tau \sim$ a few μ s
PDE at 87 K	>35% at nominal OV
High level specifications	Value
Dynamic range	1-2000 p.e.
S/N > 4	per supercell (48 SiPMs)
Trigger	1.5 p.e.

Table 4.1: DUNE requirements for the Photon Detection system.

uniform working condition for the devices, the breakdown voltage of SiPMs on the same board should be as similar as possible. Large discrepancies in the values of V_{bd} would imply different triggering value for the avalanche and thus, a loss in uniformity in the response of the Photon Detection system.

DUNE Far Detector is designed to search for extremely rare events. For this purpose, it is critical to study the different contribution to the sources of noise which could affect the devices. SiPMs working at cryogenic temperatures manifest extremely low values of dark count noise which represent one of their main strengths. On the other hand, as already described in sec. 3.9, the afterpulses probability increases at low temperature due to an increasing in the value of the quenching resistor of the devices. Therefore, a full characterization of the noise sources for the SiPMs is required before running the experiment.

Considering all the experiment requirements described above, a wide test campaign is necessary to ensure the mechanical and electrical integrity and to fulfill the quality requirements for the devices. The DUNE Single Phase Photon Detection System (SP-PDS) Consortium is responsible of testing and validating the photosensors which will be then used in DUNE Far Detector PD system.

Before the SiPMs will be produced in large number and delivered to the different group of the Consortium, a quality check control will be conducted even by the vendors. During the fabrication process, small and seemingly innocuous changes can be found in the devices. They can result in a big impact on the robustness of the SiPMs at extreme temperatures. Thus, a close cooperation with the vendor is necessary to keep notice of

any changes and ensuring a strict process control once the pre-production batch has been qualified. The vendor will be in charge of qualifying a randomly selected sample of devices from each production batch, by thermally stressing the devices and measuring their features before and after the process. Another aspect envisaged in the risk mitigation strategy for the PD system, is to limit the number of production batches.

4.2 Features of samples tested

In 2019, an agreement with two vendors has been set up by the DUNE Collaboration in view of the production of the SiPMs for first DUNE Module. The vendors are: the Italian Fondazione Bruno Kessler (FBK) and the Japanese Hamamatsu Photonics (HPK). They both agreed to optimize their SiPM technologies for the needs of DUNE and certify the sensors for operation at 87 and 77 K.

Two different technology have been down selected and are at focus in the pre-production phase:

- the Hole Wire Bond (HWB) technology of HPK implemented with Silicon package;
- the NUV-HD-Cryo (Near Ultra Violet-High Density-Cryo) technology of FBK implemented in SMD epoxy resin package.

All sensors will be produced with a surface of $6 \times 6 \text{ mm}^2$.

With these technologies, different versions will be produced. The aim of the pre-production tests is to down-select one sensor per vendor and produce 3000 SiPMs for FBK and 3000 SiPMs for HPK to be installed and tested in ProtoDUNE-SP 2.

Vendor	Split	Cell pitch (μm)	τ at 87 K (ns)
FBK	Standard	30	400
	Triple Trench	50	600
HPK	6050HS-LRQ	50	30
	6075HS-LRQ	75	63.5
	6050HS-HRQ	50	117
	6075HS-HRQ	75	254

Table 4.2: The DUNE pre-production splits.

The NUV-HD-Cryo technology developed by FBK fulfills all basic specifications for DUNE. However, it has never been implemented for

6×6 mm² sensors and with the SMD package. FBK has made a first production split of 6×6 mm² SiPMs with 30 μm cell-pitch and a recovery time of $\tau \sim 400$ ns, called the **Standard DUNE split**. Because the NUV-HD-Cryo trenches are not filled with a metal layer, this technology presents a relatively high crosstalk. A second production split has been made with a triple trench design to significantly reduce the crosstalk. This split presents three SiO₂ trenches to avoid the electrons and photons diffusion to neighbouring cells. As a disadvantage, these SiPMs could present a corresponding loss of the fill factor which is compensated by a cell-pitch (50 μm) larger than the standard DUNE split.

For Hamamatsu, the standard DUNE split is a 6×6 mm² sensor based on a low capacitance chip, with a 50 μm cell pitch and nominal metallic quenching resistance. This split is labeled as **6050HS-LRQ**. A different split with a larger cell pitch of 75 μm has been also made labeled as **6075HS-LRQ**. The recharge time of these devices are reported in tab. 4.2. As main disadvantage, the standard HPK split has a large signal amplitude of afterpulses that are likely because of the low quenching resistor and thus short recovery time. For this reason, HPK has made a two additional splits with a higher quenching resistor, 50 and 75 μm cell pitch, labeled as **6050HS-HRQ** and **6075HS-HRQ**. The recovery time of these splits are incremented by tuning the thickness and composition of the metallic resistance, assuming the reported values in Tab. 4.2.

A first batch of 25 sensors per splits have been successfully delivered to the various members of the DUNE Single Phase Photon Detection System (SP-PDS) Consortium. This batch is currently undertaking the characterization at single-SiPM level.

The next phase envisages the delivery of additional 250 sensors, already in the 6-SiPM boards that will be installed in ProtoDUNE, and perform tests at board level.

4.3 Measurements description

A tests campaign of the six different types of SiPMs described in 4.3 are currently undertaken by the various members of the DUNE Single Phase Photon Detection System (SP-PDS) Consortium. A first batch of 25 SiPMs per type have been produced. The INFN group of Bologna is one of the teams charge of the characterization of these devices. During my thesis work, collaborating with the group, I carried out in the preliminary measurements on SiPMs proposed for the PD system of ProtoDUNE-SP 2.

The SiPMs delivered to Bologna which have been subjected to testing are 4 produced by FBK with a 30 μm cell pitch and 9 by HPK, two with a 50 μm cell pitch and 7 with 75 μm cell pitch. The devices are summarized in Tab. 4.3 with their ID number of reference.

Vendor	ID	Cell pitch (μm)	Thermal cycles before shipment
FBK	14	30	18
	15	30	18
	19	30	2
	20	30	2
HPK	18	50	0
	19	50	0
	22	75	0
	23	75	0
	25	75	0
	26	75	0
	27	75	0
	28	75	0
	29	75	0

Table 4.3: SiPM samples tested.

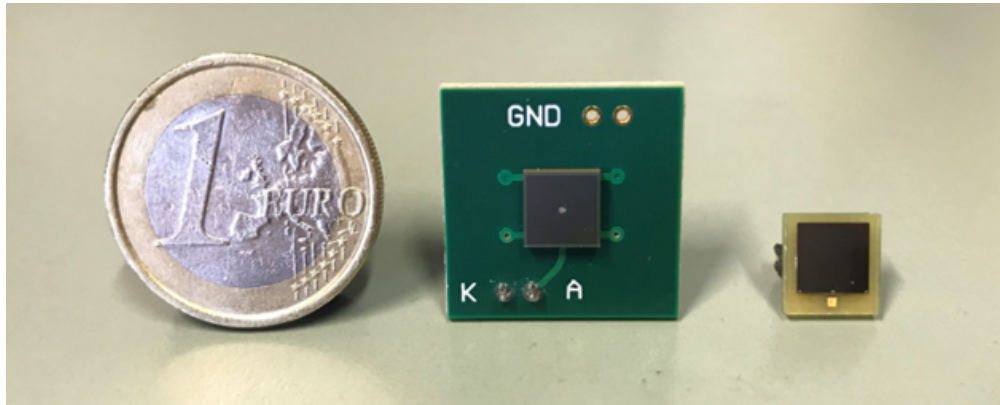


Figure 4.1: HPK SiPM (centre), FBK SiPM (right).

4.3.1 Setup description

The setup developed to perform the SiPM test campaign is shown in fig. 4.2. The cryogenic system is composed of a 5-liters dewar which can



Figure 4.2: Setup used for the characterization of the devices.

be filled with liquid Nitrogen. Thanks to a boiling point of -195.82°C (77 K), Liquid Nitrogen is exploited to create a cryogenic environment similar to that of liquid Argon (87 K). The top aperture of the dewar can be closed with a black plastic plug, which can be manually moved up and down through a mechanical system. Power and signal cables pass inside the dewar through holes drilled in the plug where the light tightness is guaranteed by a black silicon sealant or putty. All the measurements, both at room and cryogenic temperature, are performed with the SiPMs placed inside the dewar.

4.3.2 Front-end electronics

For the measurements of DCR at 77 K, each SiPM under test is powered by a preamplifier, mounted inside a metallic box (Fig.4.3). The box is vertically attached to the plug with a holder and serves to partially shield the electromagnetic external noise. A preamplification stage is necessary due to the low amplitude of the signal at cryogenic temperature. The output of the preamplifier is readout by a digital scope for the data acquisition. The amplifier is based on a SiGe transistor in common emitter configuration. The bandwidth of the amplifier is set to 340 MHz for a gain

of 3 dB at an overvoltage of 2.5 V. The gain as a function of the frequency for different applied overvoltages is shown in Fig. 4.6.



Figure 4.3: Cryogenic amplifier used for the tests in Liquid Nitrogen.

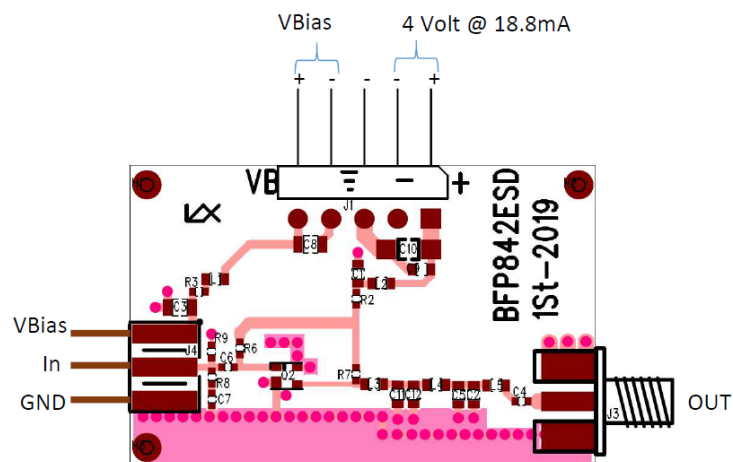


Figure 4.4: Technical scheme of the preamplifier board used in the tests.

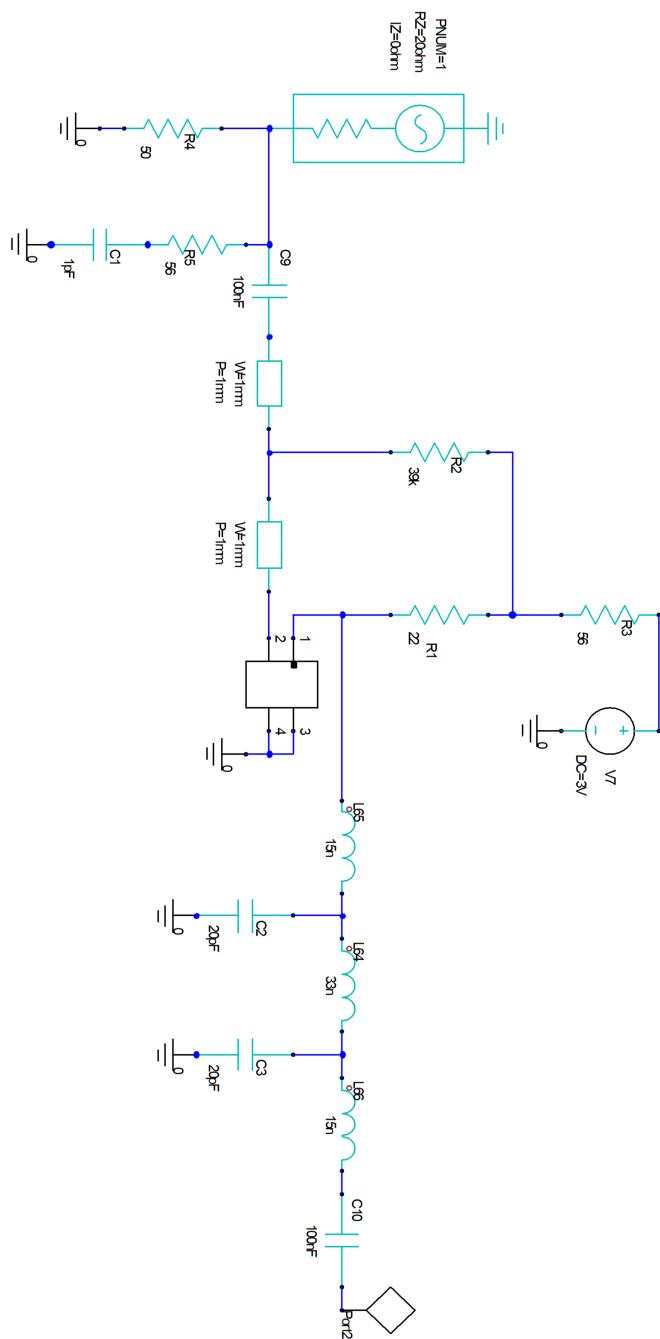


Figure 4.5: Block diagram of the preamplifier used in the cryogenic measurements.

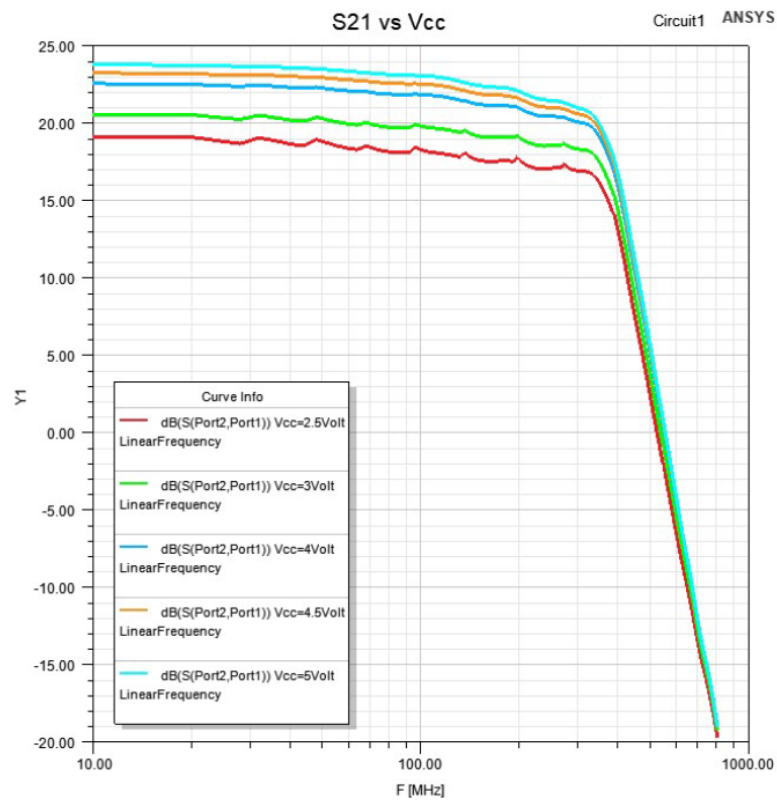


Figure 4.6: Gain of the preamplifier, as a function of the frequency for different applied overvoltages.

4.3.3 Test equipment

The current/voltage (I-V) curves of SiPM are acquired using a *Keysight B2901A Series* precision source/measure unit (Fig.4.7). It has the capability to source and measure both voltage and current, making it ideal for IV measurements. The instrument presents a broad voltage (± 210 V) and current (± 3 A DC and ± 10.5 A pulsed) sourcing capability and a resolution down to 10 fA and 100 nV [25].



Figure 4.7: The *Keysight B2901A Series* precision source/measure unit used for the I-V curves measurements.

The Dark Count Rate is measured using a *LeCroy WaveRunner 8104-MS* oscilloscope (Fig.4.8)[26]. It features four input channels, with 1 to 4 GHz Mixed Signal bandwidths and up to 40 GS/s sample rate. The single-shot acquisition sample rate for the analog channels is 10 GS/s on 4 channels and 20 GS/s on 2 channels. The repetitive sample rate is instead of 200 GS/s for repetitive signals (20ps/div to 10ns/div). The memory length of 4/2/1/ channels is 16M/32M/32M for 5000 segments acquired.

During the thermal cycles, the temperature is monitored by a PT100 temperature sensor. The PT100 has two ends, one attached inside the metallic box at the same height of the SiPM to be tested (Fig.4.9), and the other end placed at room temperature. The sensor is readout by an *Arduino board* (Fig.4.10) connected to the USB port of the oscilloscope. The temperature is recorded every 0.5 second and a temperature-time plot is created using the *Anaconda* software.

4.3.4 Thermal tests

Considering the temperature at which the SiPMs will operate in the DUNE experiment, an important aspect to be considered is their cryo-reliability. Thermal gradients stress the devices at the level of features, bonding and packaging. To verify their mechanical integrity, the sensors



Figure 4.8: The *LeCroy WaveRunner 8104-MS* oscilloscope used for the tests.

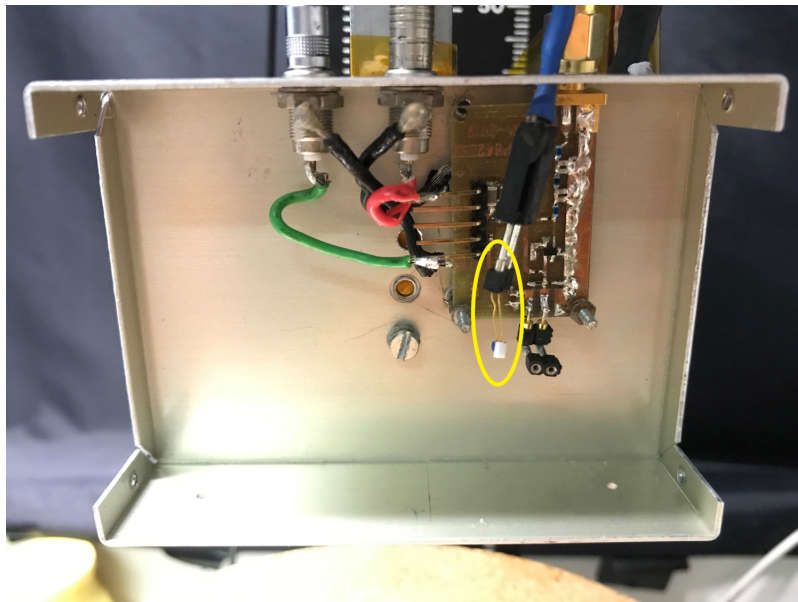


Figure 4.9: PT100 sensor for the temperature monitoring inside the dewar.

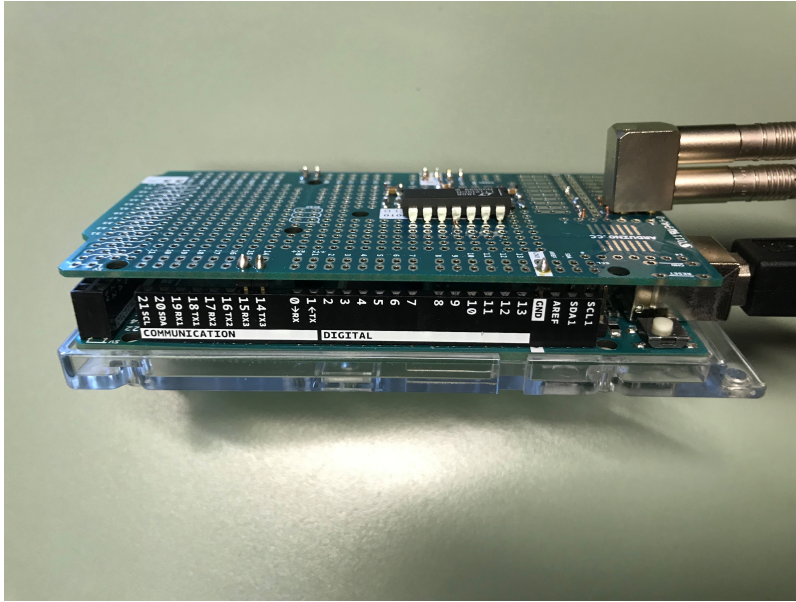


Figure 4.10: Arduino board to which the PT100 was connected.

with their packages have been tested in Liquid Nitrogen (LN) over many thermal cycles.

Operation at cryogenic temperatures changes most of the electric parameters of the SiPM. An ideal cryogenic photosensor is a device where these changes are fully reversible over all the thermal cycles. For this reason, a measurements of the SiPM features shall be carried out and after the thermal tests.

These tests therefore are aimed to evaluate both the mechanical integrity of the packaging as well as the reversibility of their features after being subjected to many thermal cycles.

Basing on the Consortium protocol, a thermal cycles consists of different phases: a first phase in which the device is expose to LN vapors for three minutes, a second one where the SiPM is submerged for ten minutes, then a phase in which it is pulled up and again exposed to LN vapors and finally a warm up phase at room temperature. Such thermal cycle should last for ~ 20 minutes per single SiPM. Each sensors had to be tested over ~ 20 thermal cycles, which implied a total time of at least ~ 400 minutes per SiPM ($\sim 6-7$ hours).

Given the huge number of devices to be tested for the full DUNE experiment, a less time-consuming procedure is envisaged. A different way to perform the test has been studied, using cycles with a total duration time of ~ 6 minutes. The different phases of a single cycle are reported

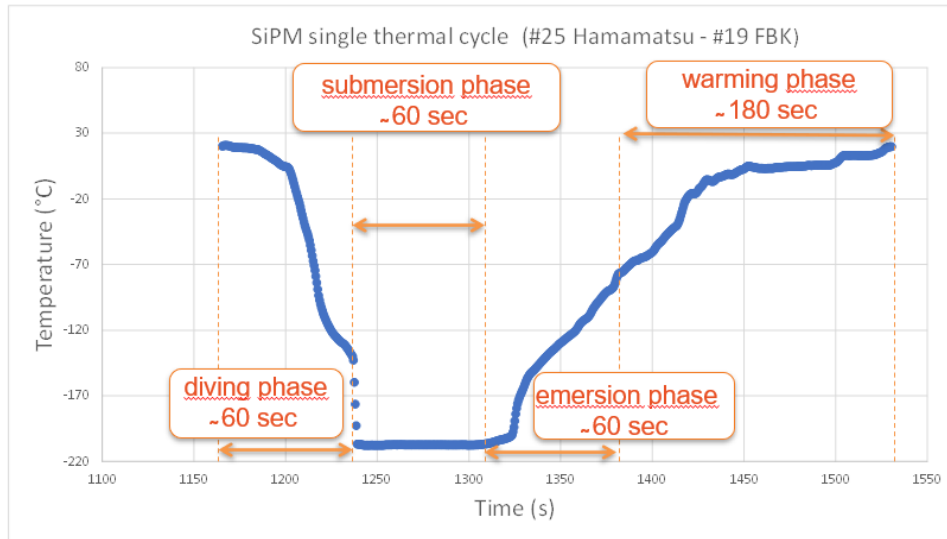


Figure 4.11: Different phases for a single thermal cycle reported with their duration time. A single cycles lasts for ~ 360 seconds (~ 6 minutes).

in Fig.4.11 divided into: a diving phase of ~ 60 seconds, a following submersion phase of again ~ 60 seconds, an emersion phase of ~ 60 seconds and finally the warming phase for ~ 180 seconds. In this latter one, to speed up the process, the SiPM was warmed with a hot air gun working at $\sim 60^\circ\text{C}$. The precision in the timing of the phases has been possible thanks to the temperature monitoring with the PT100.

Adopting thermal cycles of this type, would allow to performed a sequence of 15 cycles in ~ 1.5 hours (~ 90 minutes).

A sequence of 15 consecutive thermal cycles is reported in Fig.4.12.

4.3.5 I-V curves

During the tests, I conducted several measurements of the I-V curves for the FBK and HPK SiPMs, both at room and cryogenic temperature. Basing on the applied polarization, I studied the changing in the quenching resistance and breakdwon voltage at 77 K compared to those at room temperature.

In a forward biased configuration, the current generated in the device is initially approximately zero then, a limited exponential increasing occurs, followed by a linear growing of the current with the applied voltage. In order to conduct the analysis, the linear region has been fitted with a straigth line (Fig.4.13). The best estimate of the quenching resistance R_q

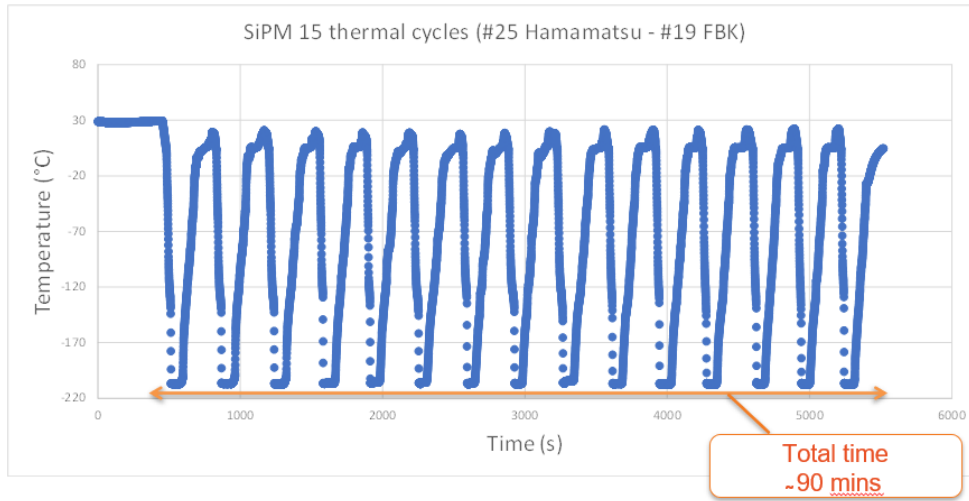


Figure 4.12: Sequence of 15 thermal cycles performed on two SiPMs at once. The total time for the complete sequence is reported.

of a single microcell is extracted as the inverse of the angular coefficient of the line:

$$R_q = \left(\frac{1}{m}\right) \cdot N_{cells} \quad (4.1)$$

where N_{cells} is the total number of pixels of the SiPM.

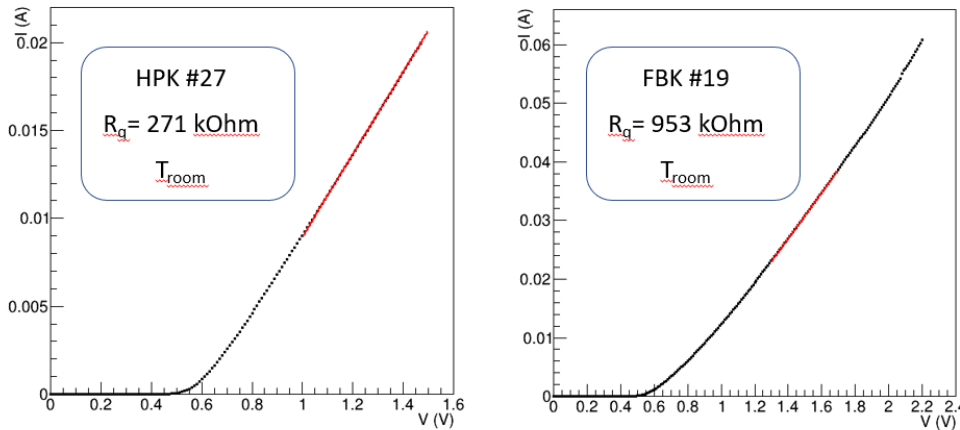


Figure 4.13: Examples of I-V curves in the forward bias polarization at room temperature (left) for a HPK sample, (right) FBK sample.

Knowing R_q is important in order to determine the influence of the afterpulses on the SiPM. During its recovery time, the fall time of the

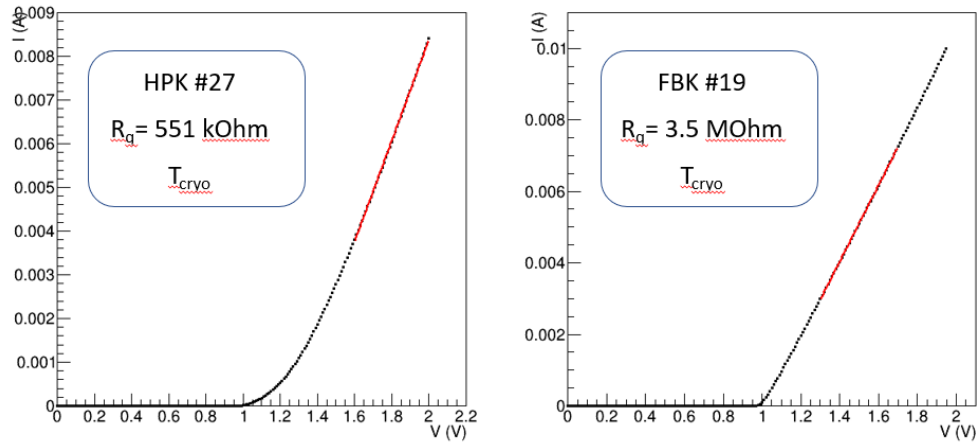


Figure 4.14: Examples of I-V curves in the forward bias polarization at cryogenic temperature (left) for a HPK sample, (right) FBK sample.

device depends on the quenching resistance. A high value of R_q implies a long recovery and thus fall time (Fig.4.15), while a lower R_q represents a shorter fall time. In the first case, because the SiPM is not yet recovered and the breakdown voltage not achieved, a potential afterpulse does not generate an avalanche. This condition mitigates the negative impact on the response of the sensor. On the other hand, an afterpulse happening when the SiPM is fully recovered and again sensible, would generate a fake signal.

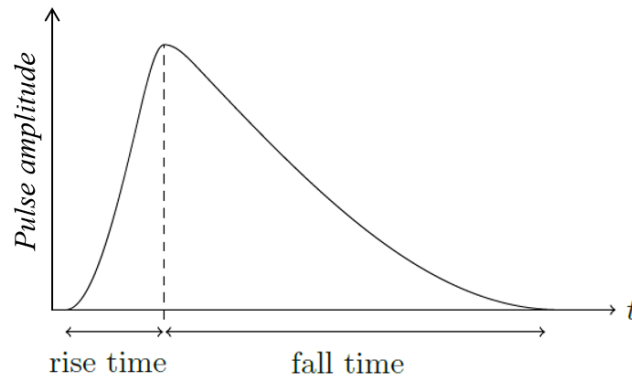


Figure 4.15: Rise time and fall time in the pulse amplitude of a SiPM.

In the reverse biased polarization, it is possible to extract the breakdown voltage of the SiPM. In this case, the value V_{bd} is identified as the intersection point between the fit on the initial linear region of the curve

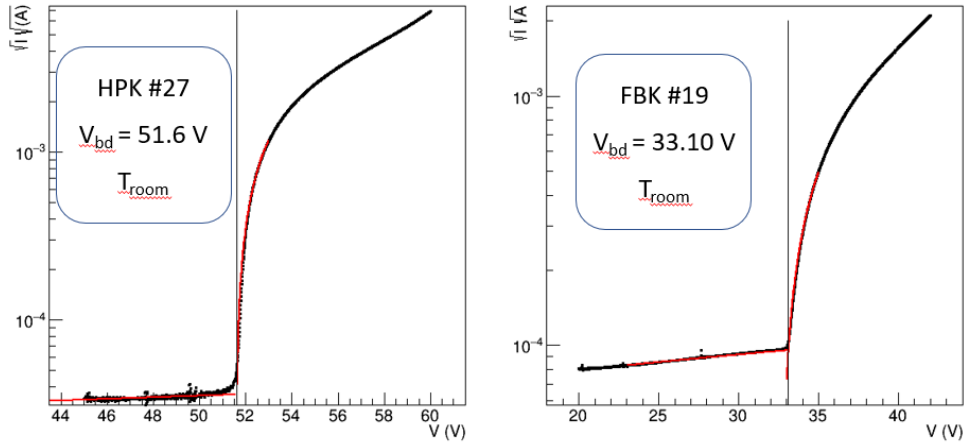


Figure 4.16: Examples of I-V curves in the reverse bias polarization at room temperature (left) for a HPK sample, (right) FBK sample.

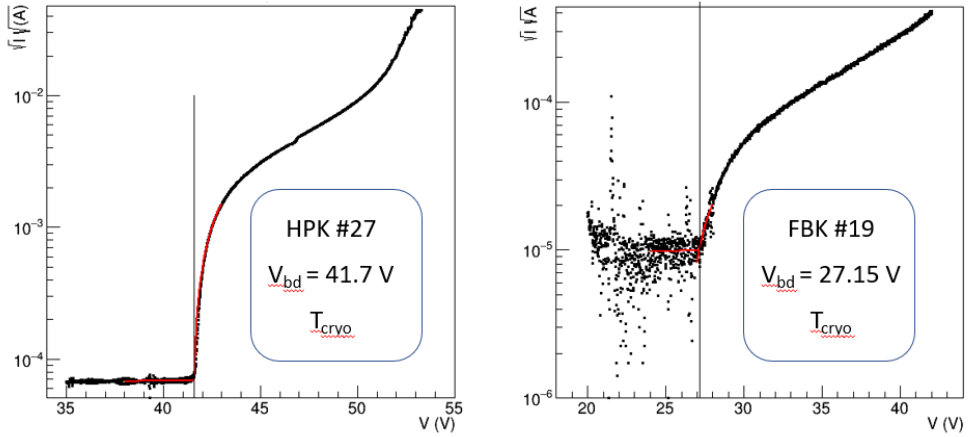


Figure 4.17: Examples of I-V curves in the reverse bias polarization at cryogenic temperature (left) for a HPK sample, (right) FBK sample.

and the fit on the following exponential region (Fig.4.16). It is important that all the samples tested manifest a uniformity in the breakdown voltages measures. This allows to gang 6 SiPMs on a same board for the next phase of test campaign, as already mentioned in sec.4.1.

Values of the quenching resistance and breakdown voltage have been measured for all the samples both at room and cryogenic temperature. The results I obtained are reported in Tab.4.4 and 4.5 and here reviewed.

At room temperature, there is a quite big difference in the quenching resistance presented for the samples made by the two vendors. The

HPK samples, being made with the Low Quenching Resistance technology (LQR), have values of R_q of the order of ~ 300 kOhm, while for the FBK samples the values are ~ 1 MOhm.

If we compare the results obtained at different temperatures, we can state that for HPK the R_q values at 77 K increases \sim twice that at room temperature. The FBK SiPMs instead, have values of R_q at 77 K which are increased by a factor of \sim four respect to that at room temperature.

In the same conditions, the values obtained for the breakdown voltage, in the case of the HPK decrease of ~ 10 V, while in the FBK case of ~ 6 V.

		T_{room}			T_{cryo}	
Vendor	ID	Cell pitch	R_q	V_{bd}	R_q	V_{bd}
HPK	18	$50\mu\text{m}$	394 k Ω	51.9 V	815 k Ω	41.9 V
	19	$50\mu\text{m}$	391 k Ω	51.1 V	812 k Ω	42.1 V
	22	$75\mu\text{m}$	277 k Ω	52.0 V	567 k Ω	42.1 V
	23	$75\mu\text{m}$	289 k Ω	51.9 V	578 k Ω	41.9 V
	25	$75\mu\text{m}$	342 k Ω	51.5 V	559 k Ω	41.7 V
	26	$75\mu\text{m}$	289 k Ω	51.7 V	613 k Ω	41.7 V
	27	$75\mu\text{m}$	271 k Ω	51.6 V	551 k Ω	41.7 V
	28	$75\mu\text{m}$	277 k Ω	52.1 V	541 k Ω	41.9 V
	29	$75\mu\text{m}$	277 k Ω	51.9 V	575 k Ω	42.0 V

Table 4.4: Results for the measurements on the HPK SiPMs at room and cryogenic temperature.

		T_{room}			T_{cryo}	
Vendor	ID	Cell pitch	R_q	V_{bd}	R_q	V_{bd}
FBK	14	$30\mu\text{m}$	986 k Ω	33.06 V	4.25 M Ω	27.00 V
	15	$30\mu\text{m}$	1.01 M Ω	33.04 V	4.46 M Ω	27.05 V
	19	$30\mu\text{m}$	953 k Ω	33.10 V	3.5 M Ω	27.15 V
	20	$30\mu\text{m}$	1.23 M Ω	33.06 V	4.78 M Ω	27.09 V

Table 4.5: Results for the measurements on the FBK SiPMs at room and cryogenic temperature.

Two SiPMs per each vendors have been subjected to a sequence of 15 thermal cycles. The features of these SiPMs have been measured before and after this procedure. The results obtained at room and cryogenic

			T_{room} , before		T_{room} , after	
Vendor	ID	Cell pitch	R_q	V_{bd}	R_q	V_{bd}
HPK	25	75 μm	342 k Ω	51.5 V	329 k Ω	51.7 V
	28	75 μm	277 k Ω	52.1 V	276 M Ω	51.8 V
FBK	19	30 μm	953 k Ω	33.1 V	956 k Ω	33.1 V
	20	30 μm	1.23 M Ω	33.06 V	1.26 M Ω	33.08 V

Table 4.6: Results for the measurements on the FBK and HPK SiPMs at room temperature, before and after 15 thermal cycles.

			T_{cryo} , before		T_{cryo} , after	
Vendor	ID	Cell pitch	R_q	V_{bd}	R_q	V_{bd}
HPK	25	75 μm	559 kOhm	41.7 V	329 kOhm	51.7 V
	28	75 μm	541 kOhm	41.9 V	276 MOhm	51.8 V
FBK	19	30 μm	3.5 MOhm	27.15 V	3.8 MOhm	27.1 V
	20	30 μm	4.78 MOhm	27.09 V	4.72 MOhm	27.07 V

Table 4.7: Results for the measurements on the FBK and HPK SiPMs at 77 K, before and after 15 thermal cycles.

temperature, along with the ID of the samples chosen, are reported in Tab.4.6 and Tab.4.7.

As a first evaluation, it appears that the devices have not changed features after this rapid thermal tests, suggesting that this new procedure can be proposed and adopted by the consortium. However, a full decision can be taken after collecting a larger statistics.

4.3.6 Dark Count Rate (DCR)

To fulfill the DUNE requirements, the Dark Count Rate of SiPMs should be <100 mHz/mm². In order to verify this requirement, measurements of the DCR have been conducted in Liquid Nitrogen. This kind of tests, due to the expected low rate of events, are relatively time consuming. Moreover, the measurements need to be conducted as much as possible in absence of light in order to guarantee the absence of real signals due to external photons. The SiPMs under test are placed inside the dewar and immersed in liquid Nitrogen. Unfortunately, our test setup is not enough to ensure a good light tightness, even when the dewar is closed with the plug. For this reason, some additional black sheets have been placed all over the vessel. To guarantee the complete absence of light, the data were acquired in a dark room with all the instruments covered with

black screens.

The FBK samples have been tested operating with an overvoltage of $V_{ov} = +4$ V while the HPK with $V_{ov} = +3$ V. Data were stored by the oscilloscope in a binary format and then converted in ROOT file and analyzed. The waveforms were acquired inside a time window of $5 \mu\text{s}$, with a division of 500 ns/div and a sampling of 1 GS/s . A trigger was set at 0.5 p.e. and a sequence of 2000 waveforms per file have been recorded. An example of the waveform acquired during a test run is shown in Fig.4.18.

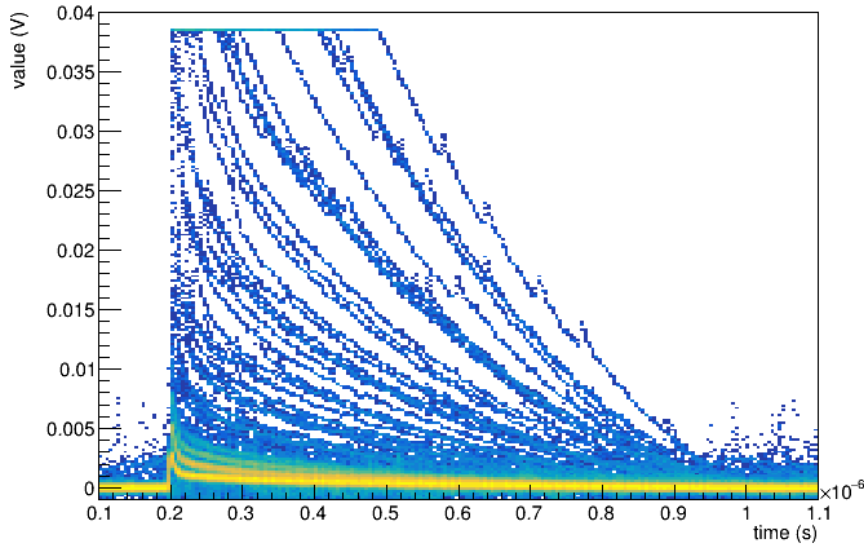


Figure 4.18: Persistence of the pulses obtained through the analysis.

The Dark Count Rate for SiPMs was extracted from the staircase curves of the samples, by fitting the linear region of the first step. From this result, the DCR per mm^2 has been calculated by dividing the DCR by the device surface.

The FBK ID 20 and HPK ID 25 have been tested running 15 thermal cycles. The measurements of the DCR is performed before and after the cycles. The results are reported in Tab.4.8.

For these samples, it has been possible also to extract the crosstalk probability. The crosstalk is evaluated as the ratio between the number of events with a pulse height larger than 0.5 p.e. and the number of events with a pulse height larger than 1.5 p.e. . Results are reported in Tab.4.9.

From the measurements of the Dark Count Rate, I evaluated the after-pulsing probability for the SiPMs under thermal test. Within an acquisi-

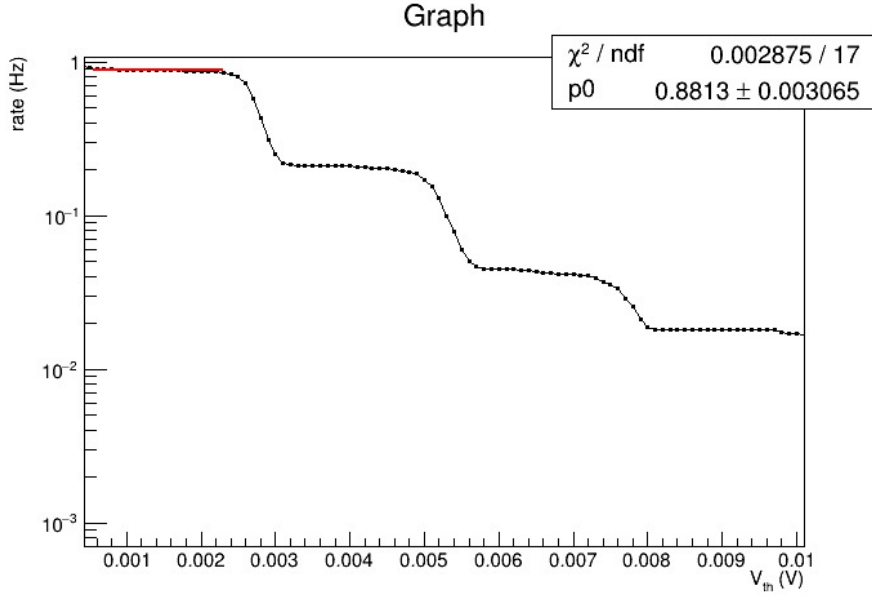


Figure 4.19: Staircase curve of the FBK ID 20. The DCR is extracted from the linear fit.

			before	after
Vendor	ID	Cell pitch (μm)	DCR (mHz/mm ²)	DCR (mHz/mm ²)
FBK	20	30	24	16
HPK	25	75	82	38

Table 4.8: Dark Count Rate of FBK and HPK samples, before and after being subjected to 15 thermal cycles.

			before	after
Vendor	ID	Cell pitch (μm)	Crosstalk	Crosstalk
FBK	20	30	24%	22%
HPK	25	75	14%	18%

Table 4.9: Crosstalk of FBK ID 20 and HPK ID 25 samples, before and after being subjected to 15 thermal cycles.

tion window of $5 \mu\text{s}$, the afterpulsing probability is defined as the number of events with one or more peaks in $4 \mu\text{s}$ after the main pulse divided by the number of main pulses. In Fig.4.20 it is shown the distribution of the time difference between two consecutive events. There are visible two

			before	after
Vendor	ID	Cell pitch (μm)	Afterpulsing	Afterpulsing
FBK	20	30	4%	6%
HPK	25	75	6%	7%

Table 4.10: Afterpulse probability of FBK ID 20 and HPK ID 25, before and after being subjected to 15 thermal cycles.

region: on the left the distribution of afterpulse events, on the right the region of dark count events.

The estimated afterpulsing probability obtained for the SiPM sample under test is reported in Tab.4.20.

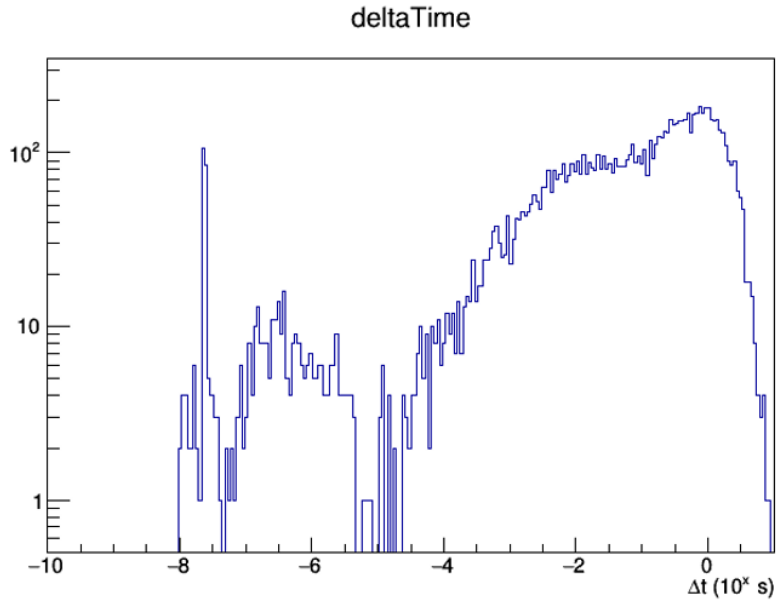


Figure 4.20: Distribution of the time difference between two consecutive events.

4.4 Future objectives

This test campaign is going to continue to increase the statistics both for the thermal tests as well as for the measurements of noise. Another aspect to investigate is the study of the gain of the devices for different overvoltages.

Once these tests will be completed, a second phase of tests should start basing on the results obtained. In this next phase the number of SiPMs will considerably increase. The splits will be composed of ~ 250 SiPMs for each technology. The sensors will be delivered already in the 6-SiPM boards that will be installed in ProtoDUNE-SP II, in order to perform tests at board level. Due to the higher number of photosensors simultaneously under test, a specific setup will be developed. Aim of this phase is to perform a full characterization of 48 SiPMs ganged together.

Conclusions

The research work presented in this thesis was carried out in the framework of the Deep Underground Neutrino Experiment (DUNE).

Neutrino oscillation plays a crucial role in the field of neutrino physics. Studying this phenomenon helps in solving some still open questions as a neutrino mass ordering and a possible CP violation in the leptonic sector. DUNE is an international project aimed to give a remarkable contribution to these topics. With its dual detectors design, a Near Detector and a Far Detector placed at a great distance, it will observe neutrino oscillation by comparing the neutrino fluxes detected at the two sites. To observe and reconstruct the neutrino interaction inside the Far Detector, DUNE will use a Photon Detection (PD) system composed of light collectors coupled with Silicon Photomultipliers (SiPM). Due to the particular working condition of the PD which will be submerged in Liquid Argon, all the photosensors need to be tested in a representative environment, in order to verify the experiment requirements.

This thesis has been focused on the characterization of the SiPMs which will be used in the Photon Detection system of future experiment prototypes. The tests carried out had the primary purpose to select a specific design and technology for the samples of SiPMs proposed. A consequent achieved goal has been the development of an experimental setup, which will represent the starting point for a following massive test campaign, necessary to validate a larger number of photosensors for the final experiments.

The samples characterized were found satisfying the DUNE requirements. In particular, the packaging of the SiPMs tested have passed the stress tests showing a good robustness over several thermal cycles. A limited number of SiPMs samples have been tested through a sequence of several thermal tests evaluating their features before and after the proce-

ture. As a first evaluation, it appears that the thermal stress to which the SiPMs have been subjected, did not change the features of the devices. However, a larger statistics is necessary to validate the procedure adopted.

The features of the SiPMs have been studied both at room and cryogenic temperature, showing a uniformity in the quenching resistance (R_q) and breakdown voltage (V_{bd}) for all the samples. The resulting values for R_q are accordant to the requested recovery time, while the uniformity found for V_{bd} is critical for the final configuration designed for the experiment. In order to reduce the number of output channels presents in DUNE, the SiPMs will be ganged in group of six on a same PCB. To ensure equal gain for all the devices on the same board biased at the same voltage, the photosensors need to present similar value of their breakdown voltage and thus a uniform response.

A study of the main sources of noise has been also reported. The results obtained are compatible with the constrain of a Dark Count Rate <100 mHz/mm² fulfilling the requirements. The Crosstalk and Afterpulse probability have been also judged acceptable.

Concluding, the results obtained during this work of thesis are encouraging, validating both the technology adopted in the production of the SiPMs as well as the experimental setup used for the measurements. A future goals will be to develop a new semi-automated setup suitable for a larger test campaign, in order to characterize at board level a larger number of SiPMs ganged in group of six on a same photosensor board.

Bibliography

- [1] W. R. Leo, "Techniques for Nuclear and Particle Physics Experiments", Springer-Verlag (1987).
- [2] Braibant S., Giacomelli G., Spurio M., "Particelle e interazioni fondamentali", Springer-Verlag (2012).
- [3] G. B. Franklin, "The KATRIN Neutrino Mass Measurement: Experiment, Status, and Outlook", in 13th Conference on the Intersections of Particle and Nuclear Physics (CIPANP 2018) Palm Springs, California, USA, May 29-June 3, 2018, 2018.
- [4] Spurio M., Particle and Astrophysics, "A multi-messenger approach", Springer-Verlag (2015).
- [5] Super-Kamiokande Collaboration (Y. Fukuda (Tokyo U., ICRR) et al.), "Evidence for oscillation of atmospheric neutrinos", Phys.Rev.Lett. 81, 1562-1567 (1998).
- [6] M. Sanchez et al., "Observation of Atmospheric Neutrino Oscillations in Soudan 2," Phys Rev D, Nov. 2018.
- [7] J. Bian, "The NOvA Experiment: Overview and Status," Presentation at the DPF 2013 Meeting of the American Physical Society Division of Particles and Fields, Santa Cruz, California, Aug. 13-17, 2013.
- [8] M. Tanabashi et al. (Particle Data Group), Phys. Rev. D 98, 030001 (2018).
- [9] J. Cao, K-B Luk, "An overview of the Daya Bay Reactor Neutrino Experiment", Preprint submitted to Nuclear Physics B, 5 May 2016, (2016).

BIBLIOGRAPHY

- [10] A. Habig, "A brief overview of MINOS neutrino oscillation results", *Modern Physics Letter A*, 15 April 2010, (2010).
- [11] KamLAND Collaboration, S. Abe et al., *Phys. Rev. Lett.* 100 (2008) 221803.
- [12] LBNE Collaboration, M. Bass et al., "Baseline optimization for the measurement of CP violation, mass hierarchy, and δ_{23} octant in a long-baseline neutrino oscillation experiment," *Phys.Rev. D* 91 no. 5, (2015) 052015.
- [13] H. Nunokawa, S. J. Parke, and J. W. Valle, "CP Violation and Neutrino Oscillations," *Prog.Part.Nucl.Phys.* 60 (2008) 338–402.
- [14] C. Adams et al., "The Long-Baseline Neutrino Experiment: Exploring Fundamental Symmetries of the Universe", in *Snowmass 2013: Workshop on Energy Frontier Seattle, USA, June 30-July 3, 2013*, 2013.
- [15] R. Acciarri et al. [DUNE Collaboration], "Long-Baseline Neutrino Facility (LBNF) and Deep Underground Neutrino Experiment (DUNE): Conceptual Design Report, Volume 1: The LBNF and DUNE Projects", 7 February 2020, (2020).
- [16] R. Acciarri et al. [DUNE Collaboration], "Long-Baseline Neutrino Facility (LBNF) and Deep Underground Neutrino Experiment (DUNE): Conceptual Design Report, Volume 4: The LBNF and DUNE Projects", 7 February 2020, (2020).
- [17] C. Amsler et al., "ArgonCube: a novel, fully-modular approach for the realization of large-mass liquid argon TPC neutrino detectors", *Tech. Rep. CERN-SPSC-2015-009. SPSC-I-243*, CERN, Geneva, Feb 2015.
- [18] Argoncube Website. <https://argoncube.org/duneND.html>.
- [19] B. Abi et al. [DUNE Collaboration], "Deep Underground Neutrino Experiment (DUNE): Far Detector Technical and Design Report, Vol1: Introduction to DUNE ", 7 February 2020, (2020).
- [20] B. Abi et al. [DUNE Collaboration], "Deep Underground Neutrino Experiment (DUNE): Far Detector Technical and Design Report, Vol4: DUNE Far Detector Single-phase technology ", 7 February 2020, (2020).

- [21] Alessandro Berra. "Silicon Photomultipliers in High Energy and Space Applications". PhD Thesis. Insubria U., Como, 2012.
- [22] P. Buzhan et al, "The Advanced Study of Silicon Photomultiplier", Proc. of the 7th Int. Conf. on ICATPP-7, 15-19 Oct. 2001, Villa Olmo Como (2012) 717.
- [23] B. Dolgoshein et al., NIM A 563 (2006) 368-376.
- [24] A. Gola et al, "NUV-Sensitive Silicon Photomultiplier Technologies Developed at Fondazione Bruno Kessler", Sensors 2019, 19, 308.
- [25] "Keysight Technologies B2900A Series Precision Source/Measure Units". In:(Feb 2018). <https://www.keysight.com/us/en/assets/7018-02794/data-sheets/5990-7009.pdf>
- [26] "Teledyne LeCroy WaveRunner 8104 Oscilloscope". <https://teledynelecroy.com/oscilloscope/waverunner-8000-oscilloscopes/waverunner-8104-r>